The vertical distribution of dust in the Martian atmosphere during northern spring and summer: Observations by the Mars Climate Sounder and analysis of zonal average vertical dust profiles

N. G. Heavens,[1,2] M. I. Richardson,[3] A. Kleinböhl,[4] D. M. Kass,[4] D. J. McCleese,[4] W. Abdou,[4] J. L. Benson,[4] J. T. Schofield,[4] J. H. Shirley,[4] and P. M. Wolkenberg[4]

Received 7 July 2010; revised 7 December 2010; accepted 3 February 2011; published 13 April 2011.

[1] The vertical distribution of dust in Mars's atmosphere is a critical and poorly known input in atmospheric physical and chemical models and a source of insight into the lifting and transport of dust and general vertical mixing in the atmosphere. We investigate vertical profiles of dust opacity retrieved from limb observations by Mars Climate Sounder during the relatively dust-clear Martian northern summer of 2006–2007 (L_s = 111°–177°of Mars year (MY) 28) and Martian northern spring and summer of 2007–2008 (L_s = 0°–180° of MY 29). To represent local maxima in inferred mass mixing ratio in these profiles, we develop an empirical alternative to the classic "Conrath profile" for representing the vertical distribution of dust in the Martian atmosphere. We then assess the magnitude and variability of atmospheric dust loading, the depth of dust penetration during these seasons, and the impact of the observed vertical dust distribution on the radiative forcing of the circulation. During most of northern spring and summer, the dust mass mixing ratio in the tropics has a maximum at 15–25 km above the local surface (the high-altitude tropical dust maximum (HATDM)). The HATDM appears to have increased significantly in magnitude and altitude during middle to late northern summer of MY 29. The HATDM gradually decayed during late summer of MY 28. Interannual variability in the dust distribution during middle to late northern summer may be connected with known interannual variability in tropical dust storm activity.

Citation: Heavens, N. G., M. I. Richardson, A. Kleinböhl, D. M. Kass, D. J. McCleese, W. Abdou, J. L. Benson, J. T. Schofield, J. H. Shirley, and P. M. Wolkenberg (2011), The vertical distribution of dust in the Martian atmosphere during northern spring and summer: Observations by the Mars Climate Sounder and analysis of zonal average vertical dust profiles, *J. Geophys. Res.*, *116*, E04003, doi:10.1029/2010JE003691.

1. Introduction

[2] Observations of the spatial and temporal variability and optical properties of atmospheric dust have been a part of almost every major spacecraft mission sent to Mars. One important achievement of this observational program has been the creation of multiannual data sets of dust column opacity with near-global coverage and repeat cycling of ~2 weeks by the Thermal Emission Spectrometer (TES) on Mars Global Surveyor (MGS) and the Thermal Emission Imaging System (THEMIS) on Mars Odyssey [*Smith*, 2004, 2009].

[3] The vertical distribution of dust has not been observed as systematically as column opacity. Mariner 9 observed the vertical distribution of dust during a global dust storm [*Conrath*, 1975; *Anderson and Leovy*, 1978]. *Jaquin et al.* [1986] used Viking Orbiter limb imagery to characterize the aerosol distribution as composed of bluish "detached" hazes that lay above a reddish "continuous" haze, which varied in height with season and latitude. They interpreted the detached hazes as water ice and the continuous haze as dust. Observations of Tharsis by instruments on the Phobos spacecraft during early northern spring suggested that dust was well mixed vertically below 25 km [*Chassefière et al.*, 1995]. More recently, limb observations from the Thermal Emission Spectrometer (TES) on Mars Global Surveyor (MGS) have been used to retrieve vertical profiles of dust during global dust storm conditions [e.g., *Clancy et al.*, 2010]; ultraviolet observations of occulted stellar light and scattered sunlight have been used to profile aerosol extinction over a very broad altitude range [*Montmessin et al.*, 2006; *Rannou et al.*, 2006]; and observations of the atmosphere at low Sun angle by Pancam on the Mars Exploration Rovers have provided limited constraints on the vertical

[1]Division of the Geological and Planetary Sciences, California Institute of Technology, Pasadena, California, USA.
[2]Now at Department of Earth and Atmospheric Sciences, Cornell University, Ithaca, New York, USA.
[3]Ashima Research, Pasadena, California, USA.
[4]Jet Propulsion Laboratory, California Institute of Technology, Pasadena, California, USA.

Copyright 2011 by the American Geophysical Union.
0148-0227/11/2010JE003691

distribution of dust within 30 km of the surface [*Lemmon et al.*, 2004].

[4] Measurements of the vertical distribution of dust in particular (as opposed to the column opacity) provide insight into the mechanisms by which dust enters and leaves the atmosphere. *Conrath* [1975] attributed the vertical distribution to the competing effects of sedimentation and vertically uniform vertical eddy diffusion. This simple picture has been complicated by (1) the possibility of additional removal processes such as the enhancement of sedimentation by the condensation of volatiles on dust particles [*Nelli and Murphy*, 2002]; (2) modeling of vertical transport above the boundary layer due to dynamical processes such as the thermal tides [*Wilson and Hamilton*, 1996]; (3) more detailed treatment of mixing within the boundary layer [*Taylor et al.*, 2007]; (4) explicit consideration in models of dust particle size and its variability [*Kahre et al.*, 2008]; and (5) consideration of the sources of dust such as mountain slope circulations [*Lee et al.*, 1982; *Rafkin et al.*, 2002] and dry convective vortices ("dust devils") [*Kahre et al.*, 2006; *Cantor et al.*, 2006; *Greeley et al.*, 2006]. Of these processes, dust devils have been the principal focus of investigation. Most of the others have been investigated by modeling, which is imperfectly constrained by observational information about the vertical distribution of dust, or have been inferred from observations of surface features modified by aeolian processes.

[5] In addition, no matter how it comes and goes, dust significantly affects the general circulation of the Martian atmosphere (and indeed circulations at all scales). Basic considerations from theory, simple nearly inviscid axisymmetric circulation models [*Schneider*, 1983] and more sophisticated terrestrial models [*Rind and Rossow*, 1984; *Wang and Rossow*, 1998] suggest that the Hadley circulation of a planet is sensitive to the vertical distribution of atmospheric heating. Solar radiation absorbed by dust during the daytime is a crucial source of diabatic heating to the lower atmosphere, influencing not only Mars's Hadley circulation but also its strong thermal tides (see *Zurek et al.* [1992] for discussion). By absorbing and emitting infrared radiation, dust, like water vapor on the Earth, either can limit or enhance the radiative cooling of the atmosphere to space. As a result, even relatively small amounts of dust can influence the circulation by enhancing the static stability [*Haberle et al.*, 1982; *Schneider*, 1983]. Thus, knowledge of the vertical distribution of dust in the atmosphere provides a key constraint for Mars atmospheric models, analogous to the constraint cloud observations provide for terrestrial atmospheric models.

[6] The effects of an enhancement in atmospheric dust on the circulation are not restricted to the location of the enhancement, which is normally Mars's lower atmosphere. Mariner 9 and later observations have shown that the winter polar middle atmosphere of Mars is much warmer than would be expected from considerations of radiative equilibrium [*Leovy*, 1982]. The Thermal Emission Spectrometer (TES) on Mars Global Surveyor (MGS) and Mars Climate Sounder (MCS) on Mars Reconnaissance Orbiter (MRO) have observed that middle atmospheric temperatures over the south pole during northern winter are 10–30 K warmer than predicted by most Mars climate models [*Smith et al.*, 2001; *McCleese et al.*, 2008], which *McCleese et al.* [2008] propose could be due, in part, to errors in the vertical distribution of dust as prescribed in or simulated by models. Modeling studies attribute middle atmospheric polar warming to adiabatic heating due to the downwelling of the Hadley circulation and connect the intensity of downwelling to the amount of dust in the atmosphere and to the level and intensity of wave breaking in the middle atmosphere [*Haberle et al.*, 1982; *Schneider*, 1983; *Barnes*, 1990; *Haberle et al.*, 1993; *Forget et al.*, 1999; *Hartogh et al.*, 2007].

[7] The Mars Climate Sounder (MCS) on Mars Reconnaissance Orbiter (MRO) has been making global, moderate vertical resolution observations of infrared radiance from Mars's limb, nadir, and off nadir in nine broadband channels sensitive to dust, temperature, and other aerosols (see *McCleese et al.* [2007] for description of the instrument and observing strategy). Simultaneous retrievals from MCS limb observations of vertical profiles of temperature, dust, and water ice are now available [*Kleinböhl et al.*, 2009a]. In terms of length of record, coverage, frequency of repeat cycling, and ability to distinguish dust opacity from water ice opacity; this data set now should be the vertical analog to the TES and THEMIS column opacity data sets.

[8] In this study, we evaluate the general characteristics and uncertainties of this data set by focusing on the vertical dust distribution during Martian northern summer, L_s = 111°–177° of Mars year (MY) 28 (2006–2007), and Martian northern spring and summer, L_s = 0°–180° of MY 29 (2007–2009). ("L_s" refers to areocentric longitude, which is the angle of the Sun-Mars vector relative to the Sun-Mars vector at northern vernal equinox and a common way of expressing the date on Mars.) To evaluate the robustness of the retrieval algorithm, retrievals from southern spring and summer of MY 29 and northern spring and summer of MY 30 (2009–2011) are discussed as well. (For a discussion of the Mars year convention used, see *Clancy et al.* [2000].) Despite the possible applications of the analytical techniques and results of this study to the prescription of the aerosol distribution in atmospheric models, we will not develop such a prescription here.

[9] Northern spring and summer are mostly exclusive of "dust storm season" (L_s = 161°–346°), as classified by *Martin and Zurek* [1993]. General weather patterns (e.g., zonal average temperature, aerosol column opacities, and the occurrence of certain types of weather systems) during this season are thought to be highly repeatable, possibly even in the wake of a global dust storm [*Richardson*, 1998; *Wilson and Richardson*, 2000; *Cantor et al.*, 2002; *Smith*, 2004]. In addition, dust column opacities are low [*Smith*, 2004, 2009], which has drawn more focus to the radiative impact of the thick water ice clouds that occur throughout the tropics and subtropics during this season rather than to that of dust [e.g., *Montmessin et al.*, 2004; *Wilson et al.*, 2008]. Nevertheless, the proposal by *McCleese et al.* [2008] that current understanding of the vertical dust distribution during this season may be incorrect requires evaluation.

[10] As the MCS retrieval algorithm has been developed further, retrieval coverage during southern spring and summer has improved greatly, including coverage before, during, and after the global dust storm in 2007. These retrievals are worthy of more detailed investigation. Interested readers

should consult *McCleese et al.* [2010], which presents the climatology of the vertical dust distribution over the entire annual cycle in less interpretive detail than this study.

[11] In section 2, we describe the retrieval data set, general aspects of the retrieval algorithm, and the significance of density-scaled opacity. In section 3, we present the vertical dust distribution at northern summer solstice in order to motivate and present a new scheme for representing vertical dust distributions compactly. In section 4, we use the scheme developed in section 3 to discuss seasonal variability and the radiative impact of the vertical dust distribution. In section 5, we summarize our results. In the companion paper, *Heavens et al.* [2011] (hereafter called P2) use a combination of data analysis and simple modeling to consider the implications of the major results of this study for dust lifting and transport processes.

2. Data and Basic Analysis

2.1. Retrieval Characteristics

[12] Atmospheric retrievals from MCS observations consist of vertical profiles of temperature, T, (K), dust opacity, i.e., fractional extinction due to dust per unit height, $d_z\tau$, (km^{-1}) at 463 cm^{-1} (the center of MCS's A5 channel), and water ice opacity (km^{-1}) at 843 cm^{-1} (the center of MCS's A4 channel), gridded on pressure, p, coordinates. The vertical resolution of these profiles is ~5 km. Each retrieved profile is also associated with an uncertainty profile based on the estimated detector noise and misfit of the observed radiance by the forward model of the retrieval. For $d_z\tau > 10^{-5}$ km^{-1}, the estimated uncertainty in $d_z\tau$ is typically less than 10%. Altitude data gridded on pressure coordinates, which is based on the geometric pointing of the instrument, is also available for each profile (see examples in Figures 4 and 17). The uncertainty in the altitude data is +/− 1 km. The pressure at the surface, p_s (Pa) can be extrapolated from the pressure retrieval using the hydrostatic equation. This extrapolated surface pressure should be used cautiously, since it is subject to uncertainties in both the altitude data and the temperature profile between the lower end of the retrieval and the surface. Where possible, surface temperature, T_0 (K), is also retrieved. *Kleinböhl et al.* [2009a] provide a history of data and retrieval coverage, a description of the retrieval algorithm, and an evaluation of its performance under different observational conditions. The observations analyzed here use a version of the retrieval algorithm that includes a single scattering approximation described by *Kleinböhl et al.* [2009b, also A single scattering approximation for infrared radiative transfer in limb geometry in the Martian atmosphere, submitted to *Journal of Quantitative Spectroscopy and Radiative Transfer*, 2010]

[13] Temperature and opacity profiles are retrieved by generating forward models of the radiance measurements performed by MCS. In the retrievals analyzed here, the modeled radiance measurements are of limb emission in the A1, A2, and A3 channels, which primarily are sensitive to emission by CO_2 in the 15 μm absorption band and thus to temperature and pressure; limb emission in the A4 channel, which is primarily sensitive to emission by water ice; limb emission in the A5 channel, which is primarily sensitive to emission by dust; and nadir/off-nadir emission in the B1 channel, which is primarily sensitive to surface temperature. The retrieval algorithm has been designed to confront two fundamental problems with modeling limb emission. If a limb measurement includes a substantial portion of the surface in its field of view, surface radiance will be a significant part of the total radiance. Uncertainties in the modeling of the surface emission at a zenith angle close to 90° may introduce errors in the retrieved atmospheric quantity. Second, if the line-of-sight (LOS) opacity in the limb is high, the emission will approximate that of a blackbody. Thus, relatively significant differences in limb opacity, which would have produced large fractional changes in observed radiance in the optically thin case, will produce relatively small fractional changes in the observed radiance, leading to higher uncertainty in the retrieved quantity.

[14] Therefore, the MCS algorithm requires that the lowest detector used in the retrieval of dust must have a LOS opacity less than 1.9 (equivalent, though dependent on the distribution of aerosol in the limb path, to a retrieved opacity of ~4×10^{-3} km^{-1}) and a contribution of less than 10% from the surface in the detector field of view (FOV). The practical effect is that retrieved vertical profiles of dust (with rare exceptions) do not include information from detectors observing limb paths less than ~8 km above the surface.

[15] In some cases, retrieved profiles only use information from detectors observing at levels higher than ~8 km above the surface, further limiting information about low-level dust. This feature can arise from the LOS opacity limit, but it also can arise from evaluation of the goodness of fit of the observed radiances by the forward model. If the goodness of fit is sufficiently poor, temperature or aerosol will not be reported at the level of the atmosphere where the observed radiance is misfit, an action typically called "rejection." If rejection of detectors occurs too high in the atmosphere, the entire retrieval will be rejected. These misfits likely arise from errors in the spectroscopy of the gas or aerosols used by the forward model. Since the spectroscopic properties of the gas are well known from laboratory experiments, the spectroscopy of the aerosols is most likely at fault. These uncertainties have been minimized by assuming different aerosol size distributions (a major uncertainty in aerosol spectroscopy) and retrieving from sample observations over the full range of latitude, season, and time of day. The size distributions that minimized misfit globally then were used to retrieve the entire data set. This approach, however, may introduce errors if the size distributions vary significantly with altitude, latitude, season, or time of day.

[16] Underestimating aerosol size could be a critical source of uncertainty. Larger ice and dust particles are more strongly scattering in the thermal infrared [*Wolff and Clancy*, 2003]. The retrieval algorithm already accounts for the contribution to the observed radiance of weaker scattering by the particles of the assumed size distribution. In addition, when nadir or off-nadir views are available, the surface emission that is the primary source of the scattered radiation can be constrained. However, if an aerosol's single scattering albedo is underestimated, the retrieval algorithm will underestimate the radiation scattered by aerosols and interpret it as emission, which will result in a systematic error in the retrieved opacity. An erroneous size distribution of one aerosol type also could introduce a systematic error in the retrieval of another aerosol type. However, significant differences between the true and assumed particle size dis-

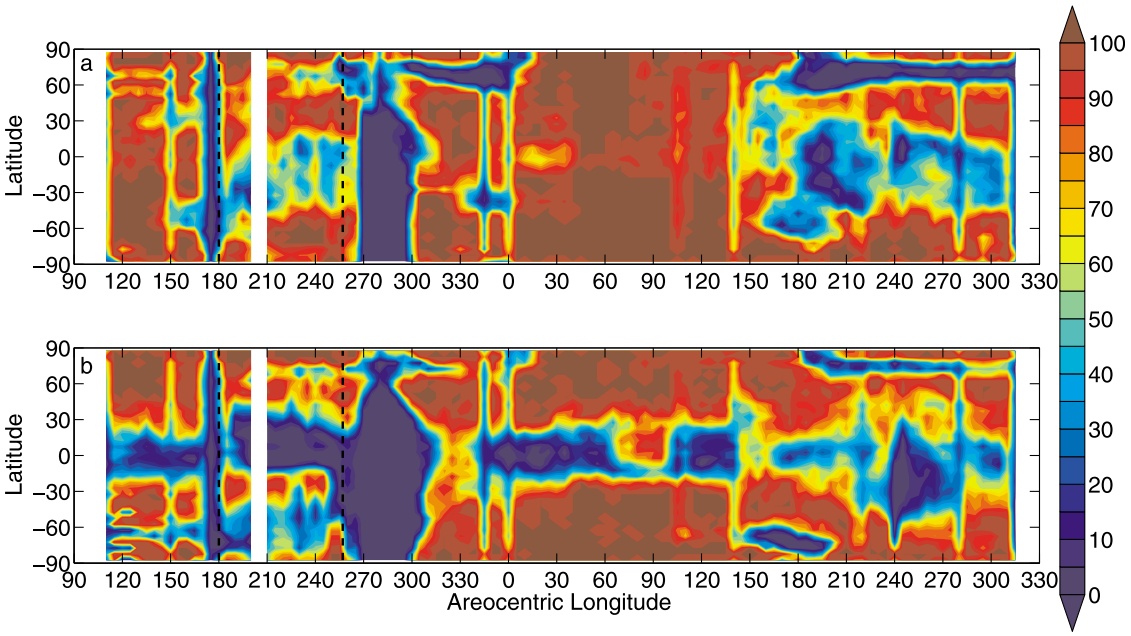

Figure 1. (a) Percentage of longitudes in the binning scheme described in section 2.2 sampled by nightside retrievals versus latitude and L_s during MY 28 and MY 29. (b) Percentage of longitudes in the binning scheme described in section 2.2 sampled by dayside retrievals as a function of latitude and L_s during MY 28 and MY 29.

tributions are likely to result in partial or full rejection of the retrieved profile.

[17] A small number of retrievals from late northern summer of MY 28 are generally omitted from this analysis. Between 9 February 2007 and 14 June 2007 (L_s = 180°–257° of MY 28), MCS operated in a mode known as "limb staring" in which the limb was observed at a constant angle relative to the spacecraft. This degraded mode of operation primarily affects the altitude range of the atmosphere observed by the instrument and the calibration of the data. Therefore, retrievals from data collected from this period provide less information about high altitudes in the southern hemisphere and low altitudes near the north pole than retrievals from data collected when the instrument was scanning the limb. In addition, retrievals from limb-staring data have greater uncertainties in areas of the atmosphere where radiances are low due to uncertainties in the calibration of the instrument in limb-staring mode. Agreement between retrievals from limb-staring and nominal limb-scanning retrievals are reasonable [*Kleinböhl et al.*, 2009a], but the limited vertical range of limb-staring retrievals (and hemispheric differences in the vertical range) makes reconstruction of the dust distribution more difficult.

2.2. Zonal Averaging and Derived Quantities

[18] To reduce biasing of zonal averages by uneven observational sampling in longitude, retrievals are separated into "dayside" (0900–2100 LST) and "nightside" (2100–0900 LST) bins and further binned in 36 (5° resolution) mean latitudinal bins, 64 (5.625° resolution) mean longitudinal bins, and L_s bins at 5° resolution. Mean latitude and longitude refer to the coordinates at the tangent point observed by the center of the MCS detector array at ~40 km above the surface. While averaging in this way reduces the bias due to uneven population of retrievals with longitude, it does not avoid the bias that arises if some longitudes have no retrievals. Since the conditions under which unsuccessful retrieval occurs are quite variable, the uncertainty in the zonal averages due to the exclusion of information from unsampled longitudes is very difficult to estimate.

[19] Aerosol opacity at a particular pressure level will not be reported in all retrievals in a particular bin, so additional caution must be exercised when averaging. Unreported aerosol at the higher pressure end of the retrieval is expected to be the result of high LOS opacity, proximity to the surface, and/or errors in aerosol spectroscopy. Thus, in the averaging process, the unreported aerosol opacity at the higher pressure end of the retrieval is not included, that is, the average aerosol opacity at 200 Pa is the average of all aerosol opacities reported at 200 Pa. But at the lower pressure end of the retrieval, opacity is usually not reported because the emitted radiance due to aerosol is small relative to detector noise and/or radiance from the wings of the instrument field of view, implying that the aerosol opacity is small. In rare cases, opacity is reported at a very low pressure level in the atmosphere. Averaging all reported opacities in that case would result in an average opacity that is unrealistically high. Thus, aerosol opacity above the lowest pressure at which aerosol opacity is reported is treated as if zero opacity were reported.

[20] The variability in the longitudinal sampling of the zonal averages described above is depicted in Figures 1a and 1b. Longitudinal sampling is controlled by a variety of other factors, e.g., periods in which data was not collected because the instrument was stowed. The absolute breaks in coverage in an L_s bin are indicated in white. For example, the break at L_s = 210° during MY 28 is a period

during which the instrument was stowed. For reasons discussed in section 3.2, dayside coverage over the equator is very limited throughout much of northern spring and summer.

2.3. A5 Channel Opacity and the Utility of Density-Scaled Opacity

[21] Opacity in the A5 channel is the retrieved quantity related to dust that follows most directly from MCS observations of radiance. The assumed size, shape, and composition of dust particles used in the retrieval algorithm yields a conversion factor between A5 channel opacity and visible opacity at 600–700 nm of ~7.3. This factor differs from the conversion factor of 4.4 reported by *Kleinböhl et al.* [2009a], because it accounts for the higher visible/infrared opacity ratio of smaller (effective radius of 1.06 μm versus 1.5 μm) dust particles now assumed by the retrieval algorithm. If knowledge of the properties and/or spectroscopy of atmospheric dust and of their spatial and temporal variability improves in the future, such conversions will be made with greater confidence.

[22] Given assumptions of the size, shape, and composition of dust particles, opacity can be converted to three quantities: volumetric number density, N_v; mass number density, N_m; and mass mixing ratio, q. For consistency's sake, let us use the same assumptions as the retrieval algorithm: that the dust is compositionally uniform and made of spherically symmetric particles with a modified gamma size distribution of the form

$$n(r) \propto r^{a} \exp(-br^{c}) \tag{1}$$

Past modeling of the decay of a global dust storm suggests that Martian dust particles are not spherical but are actually thin disks [*Murphy et al.*, 1990]. *Wolff and Clancy* [2003], however, have shown that the extinction cross sections of moderately oblate (disks) or prolate spheroids are nearly identical to the extinction cross sections of spheres in the portions of the spectrum used for aerosol retrieval by the MCS retrieval algorithm.

[23] The opacity as a function of the volumetric number density, N_v, is [e.g., *Taylor et al.*, 2007]

$$d_z\tau = \int_0^\infty Q_{ext}\pi r^2 N_v n(r) dr \tag{2}$$

In equation (2), Q_{ext} can be treated as a function of the integrated dust size distribution rather than radius and can be extracted from the integral along with π and N_v, such that

$$N_v = \frac{d_z\tau}{Q_{ext}\pi \int_0^\infty r^2 n(r) dr} \tag{3}$$

The value of Q_{ext} used by the retrieval algorithm is 0.35, which is obtained from Mie theory as described by *Kleinböhl et al.* [2009a].

[24] The term $\pi\int_0^\infty r^2 n(r) dr$ in equation (3) is the average geometric cross section of the distribution, G. So equation (3) becomes

$$N_v = \frac{d_z\tau}{Q_{ext}G} \tag{4}$$

where G is assumed to be 1.26 $(\mu m)^2$ in the retrieval algorithm. So $N_v[m^{-3}] = 2.3 \times 10^9\, d_z\tau[km^{-1}]$. The mass number density, N_m, then can be obtained by dividing N_v by the atmospheric density, ρ.

[25] The mass mixing ratio is obtained similarly. Scaling equation (3) by ρ, we obtain the density-scaled opacity:

$$\frac{d_z\tau}{\rho} = \frac{N_v Q_{ext}\pi}{\rho} \int_0^\infty r^2 n(r) dr \tag{5}$$

We can form an expression for the mass mixing ratio by calculating the ratio between the mass of dust particles in a given volume and the mass of air in the same volume:

$$q = \frac{\rho_D N_v \int_0^\infty \frac{4}{3}\pi r^3 n(r) dr}{\rho} \tag{6}$$

Equations (5) and (6) can be combined so that

$$q = \frac{4}{3}\frac{\rho_D}{Q_{ext}}\frac{d_z\tau}{\rho}\frac{\int_0^\infty r^3 n(r) dr}{\int_0^\infty r^2 n(r) dr} \tag{7}$$

The integral ratio above is equal to "the effective radius," r_{eff}, which is 1.06 μm for the size distribution used by the retrieval algorithm. So

$$q = \frac{4}{3}\frac{\rho_D}{Q_{ext}}\frac{d_z\tau}{\rho} r_{eff} \tag{8}$$

Assuming ρ_D = 3000 kg m^{-3}, q (ppm) = $1.2 \times 10^4\, d_z\tau/\rho$ (m^2 kg^{-1}).

[26] Conversions between density-scaled opacity and mass mixing ratio are somewhat affected by uncertainties in dust particle size. If equation (8) is rearranged, $d_z\tau/\rho$ is proportional to the product of Q_{ext}/r_{eff} and q. The parameter Q_{ext} is dependent on the size distribution, so that if there is significant particle size segregation in the atmosphere, variability with size in Q_{ext}/r_{eff} could result in inferring an apparent enhancement of mass mixing ratio above the surface when no enhancement is actually present. For example, if small dust particles lie over large ones and Q_{ext}/r_{eff} is significantly larger for small particles, a given mass mixing ratio of small particles will have greater opacity than the same mass mixing ratio of large particles. Table 1 shows the results of Mie scattering simulations of Q_{ext} for dust size distributions with different r_{eff} but the same effective variance as the size distribution used by the retrieval algorithm. The variability in the ratio over a reasonable size range for dust is no more than 30%. Note that the segregation of submicron particles over greater than micron-sized particles will produce an apparent depletion of mass mixing ratio in a truly uniformly mixed profile. The reverse segregation is physically implausible, because of the inverse relationship between sedimentation velocity and particle radius, so an extremum in dust density-scaled opacity also is an extremum in mass mixing ratio.

[27] The rough interchangeability of mass mixing ratio and density-scaled opacity is useful for understanding the

Table 1. Results of Mie Scattering Simulations That Show the Sensitivity of Q_{ext}/r_{eff} in the MCS A5 Channel to Dust Particle Size

r_{eff} (μm)	Q_{ext}/r_{eff} (μm^{-1})	Q_{ext}/r_{eff} Normalized by the Value at 1.06 μm
0.75	0.3095	0.970
1.06	0.3305	1.00
1.50	0.3619	1.10
2.12	0.3956	1.20
3.00	0.4137	1.25
4.24	0.3998	1.21
6.00	0.3524	1.07

radiative and dynamical significance of particular vertical profiles of dust. In an optically thin atmosphere (even for nonuniform dust), the quantity $d_z\tau/\rho$ is also proportional to the unit heating rate per unit mass due to dust at fixed wavelength, J. Thus, the dust mass mixing ratio (outside of dust storm conditions) is a good proxy for the diabatic heating rate due to dust and vice versa.

3. A New Scheme for Representing Martian Vertical Dust Distributions

3.1. Background

[28] *Conrath* [1975] considered the competing effects of sedimentation and mixing during a global dust storm and derived that the profile of mass mixing ratio of dust in the atmosphere should be

$$q = q_0 \exp\left[\nu\left(1 - \sigma^{-1}\right)\right] \tag{9}$$

where q_0 is the mass mixing ratio at the surface, ν is the ratio between the characteristic dust diffusion time and the characteristic dust sedimentation time at the surface (the Conrath parameter), and σ is $\exp(-z/H)$, where z is height and H is atmospheric scale height. In the isothermal approximation of the atmospheric pressure and density profiles generally used by *Conrath* [1975] and in a coordinate system with pressure at the top of the domain (p_{top}) that is sufficiently small, this definition of σ is approximately equal to the definition of σ used in atmospheric models for the coordinates of the vertical computational grid:

$$\sigma = \frac{p - p_{top}}{p_s - p_{top}} \tag{10}$$

When used in an atmospheric model [e.g., *Forget et al.*, 1999], a pseudo σ, $= p/p_0$, is often substituted for σ in equation (9), where p_0 is a reference pressure, e.g., 700 Pa [*Forget et al.*, 1999], below which q is taken to be q_0.

[29] *Forget et al.* [1999] modified this scheme of *Conrath* [1975] using analyses of Mariner and Viking data by *Anderson and Leovy* [1978] and *Jaquin et al.* [1986] to account for the seasonal variability in the height of observable dust in the atmosphere:

$$q = q_0 \exp\left[\nu\left(1 - \tilde{\sigma}^{-l}\right)\right] \tag{11}$$

where l is equal to the ratio between a reference height, Z_0, and the maximum height of observed dust, $z_{\max}$, which is a function of latitude and areocentric longitude (L_s). The value of ν (0.007) used by *Forget et al.* [1999] is derived from the observation by the Mariner 9 television camera that dust reached a height of at least 50 km above the surface during the 1971 global dust storm.

[30] The column opacity, τ, is the integral of equation (9) or (11) with height from the top of the atmosphere to the level of interest. But as first described by *Conrath* [1975], the resulting optical depths involve exponential integrals, which are computationally expensive. Thus, the GCM described by *Forget et al.* [1999] computes optical depth as

$$\tau = \tau_0 \tilde{\sigma} \exp\left[\nu\left(1 - \tilde{\sigma}^{-l}\right)\right] \tag{12}$$

which is obtained using a similar procedure to the exact integration by assuming that the exponential function in equation (11) is a constant (a suitable approximation for $\nu = 0.007 \ll 1$) and incorporating H, ρ_0, and q_0 into a reference optical depth, τ_0.

3.2. Maxima in Dust Density-Scaled Opacity Profiles

[31] MCS dust profiles suggest that the vertical distribution of dust needs to be represented compactly by some scheme other than those of *Conrath* [1975] and *Forget et al.* [1999]. Figures 2a and 2b show zonal averages of nightside retrievals from L_s = 87.5°–92.5° (hereafter called L_s = 90° for shorthand) during MY 29 and MY 30 of the zonal average density-scaled opacity. Figure 2c replicates the dust distribution of the MY 24 scenario of the Mars Climate Database [*Forget et al.*, 2001; *Montmessin et al.*, 2004] at L_s = 90°. This scenario uses the vertical distribution given by equation (11). Note that (1) q_0 (in terms of density-scaled opacity) is $g/P_0\ \tau_0$, where g is the acceleration due to gravity and P_0 is the reference surface pressure of 700 Pa; (2) τ_0 is scaled to account for the assumed visible/infrared MCS dust opacity ratio and the visible/9 μm opacity ratio used by *Forget et al.* [1999]; and (3) the dependence of τ_0 on latitude and L_s is that given by *Montmessin et al.* [2004]. The well-mixed profiles of dust density-scaled opacity from the surface up to some pressure produced by the modified Conrath scheme of *Forget et al.* [1999] contrast markedly with the observed zonal average profiles with maxima in density-scaled opacity at ~60 Pa observed in the MCS retrievals near the equator and both poles. In MY 29, the zonal average density-scaled opacity at the highest pressure levels with reported opacity is a factor of four smaller than the density-scaled opacity maximum (Figure 2a). In MY 30, opacity is reported at higher pressures than in MY 29, and the enhancement of density-scaled opacity at ~60 Pa relative to the near-surface value is up to a factor of 10 (Figure 2b). On the whole, the zonal average dust distributions at northern summer solstice of both years are very similar on their common vertical range. For instance, a region of dust-clear air near 60°S is apparent in both Figures 2a and 2b.

[32] The enhancement at 60 Pa, the high-altitude tropical dust maximum (HATDM), in the zonal average of dust density-scaled opacity is due to the high number of individual dust profiles from the tropics with resolved enhancements (maxima) in dust density-scaled opacity. Figure 3 shows the distribution of the difference in altitude (calculated from the pointing of the instrument) between the lowest level of the profile at which dust is reported and the level of

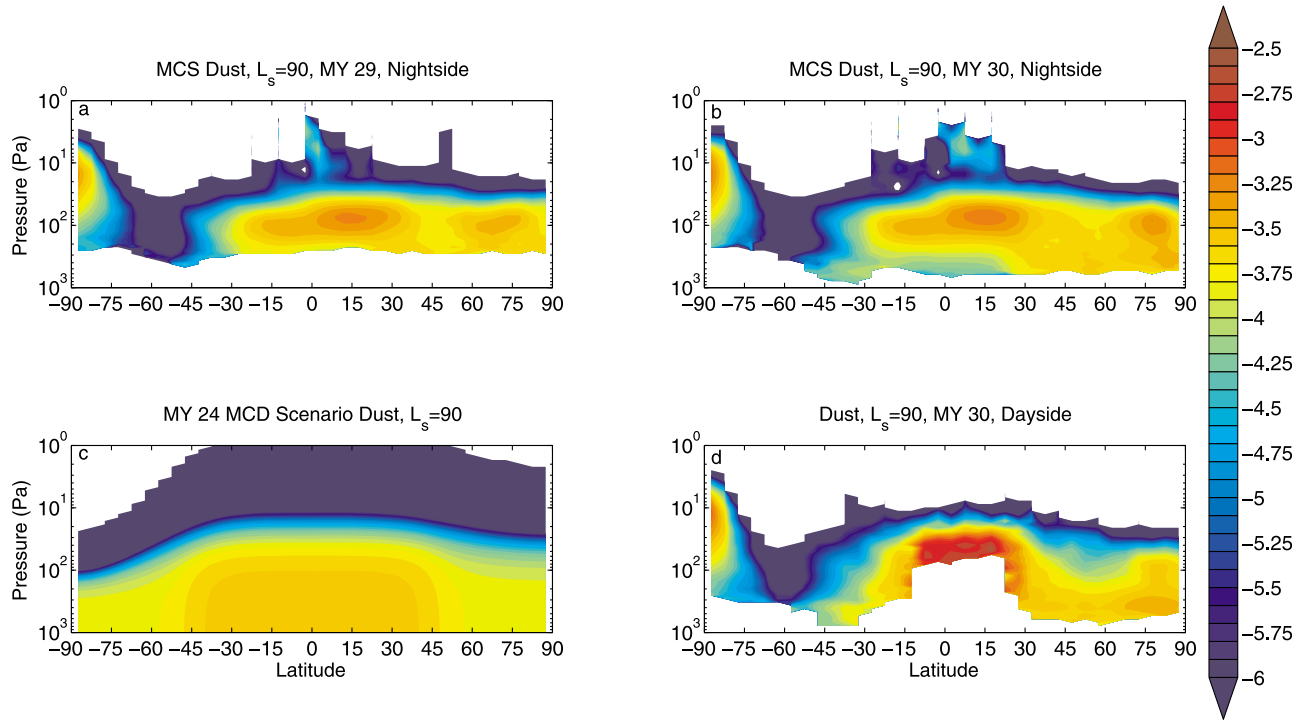

Figure 2. Log_{10} of zonal average dust density-scaled opacity ($m^2\ kg^{-1}$) as labeled. See text for further discussion. Contours are every 0.1 log units. White space below the colors indicates no data. White space above the colors and the darkest blue indicates density-scaled opacity below $10^{-6}\ m^2\ kg^{-1}$.

the maximum dust density-scaled opacity for all individual retrievals from 20°N–25°N, MY 30 on the nightside (where the peak dust density-scaled opacity within the HATDM occurs in Figures 2a and 2b). 95% of retrieved profiles have a maximum in dust density-scaled opacity at least 5 km above the lower end of the retrieved profile. The typical difference is ~15 km. Thus, the HATDM at northern summer solstice usually is resolved within the vertical range of individual MCS retrieved profiles. Individual dust profiles with resolved maxima are shown in Figures 4a–4d (see Table 2). Two of these profiles have resolved maxima in both opacity and density-scaled opacity, and all of them are cut off at ~5 km above the local surface.

[33] The dayside dust distribution at northern summer solstice is somewhat different from that of the nightside. Figure 2d shows the dayside zonal average dust density-scaled opacity at L_s = 90°, MY 30. The dayside and nightside (Figure 2b) dust distributions are fairly similar outside the tropics, but between 15°S and 30°N, dust density-scaled opacity at 60 Pa averages 3 times higher than on the nightside, and there is no reported opacity at pressures higher than ~100 Pa. Figures 4e–4h show three individual profiles from northern summer solstice of MY 30 near Olympus Mons, each retrieved from data around 12 h apart. Unlike the other profiles in Figure 4, the estimated altitude of the surface differs significantly between each profile. The surface is 4 km, −1 km, and 13 km above the MOLA datum for the opacity profiles in Figures 4e, 4f, and 4g, respectively, so the maximum in Figure 4e is ~5 km below the maximum in Figure 4g in geometric space. The nightside profiles both have resolved maxima and are cutoff ~5 km above the local surface. The intervening dayside profile is cut off at ~30 km above the local surface at a maximum opacity roughly equivalent to the LOS opacity limit mentioned in section 2.1 and a maximum density-scaled opacity around 3 times larger than the resolved maxima in the nightside profiles. As might be expected from the zonal average distribution, these features are typical of dayside profiles at northern summer solstice, which, if they are not cut off at high values of dust opacity, are cut off at high values of water ice opacity. The large and growing uncertainty at the lower end of the opacity profile in Figure 4f is a good example of uncertainty growing as limb opacity increases (section 2.1).

[34] A significant contrast in dustiness between the dayside and nightside distributions is typical in the northern tropics during most of northern spring and summer. Figures 5a and 5b show the nightside and dayside zonal average dust density-scaled opacity at 20°N–25°N during MY 28 and MY 29 (including those from limb-staring observations). (Note the decay in dust concentrations after the 2007 global dust storm during late southern summer of MY 28.) Figures 5c and 5d show the sampled longitudinal bins (colored red) used to create the zonal averages. Outside of northern spring and summer, agreement between nightside and dayside zonal averages at this latitude is generally good. For instance, just before southern summer solstice of MY 29, the vertical dust distribution on both the dayside and nightside has a uniform value of density-scaled opacity ($8 \times 10^{-4}\ m^2\ kg^{-1}$) up to 20 Pa. During the increase in dust concentration and depth of penetration during late northern summer of MY 29, nightside and dayside agreement is similarly good. It is only between L_s = 45° and L_s = 135° that the distributions differ as in Figures 2b and 2d.

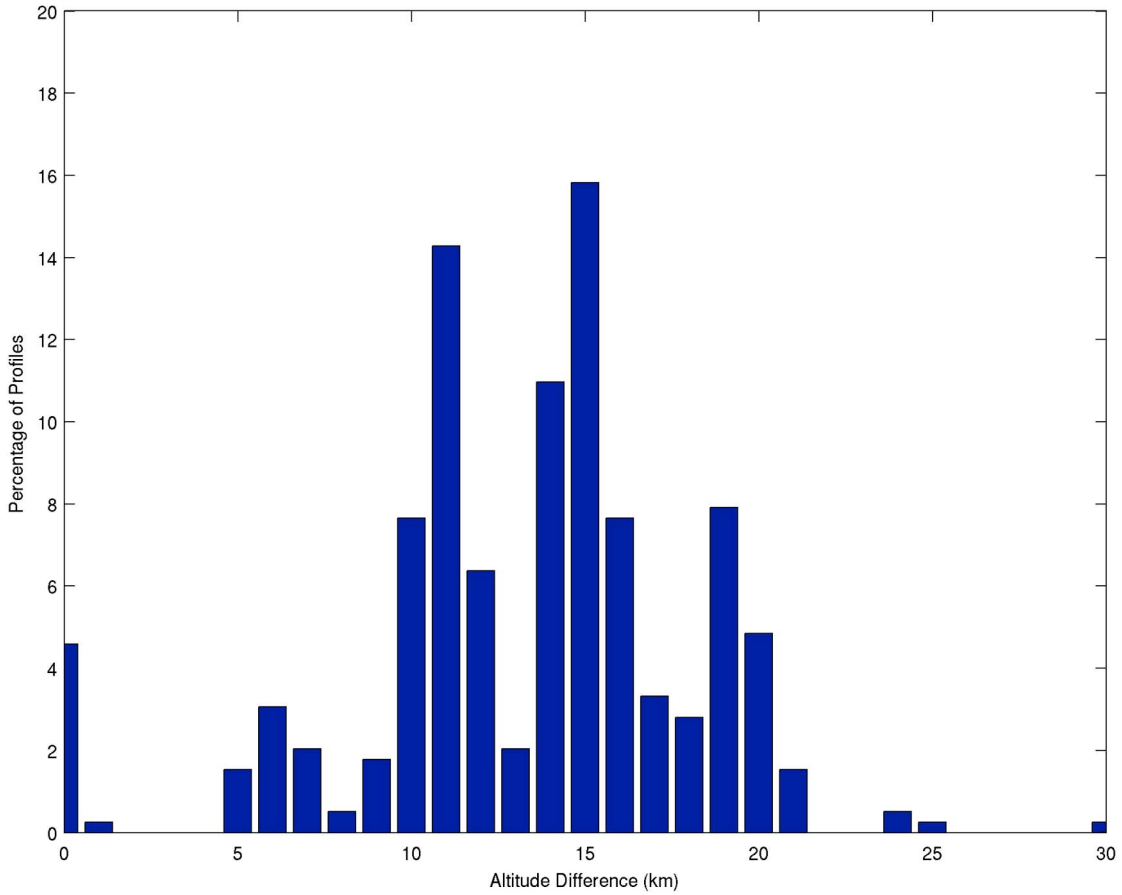

Figure 3. Histogram of the difference between the lowest altitude (relative to the Mars Orbiter Laser Altimeter datum) at which dust opacity was reported and the altitude at which the highest dust density-scaled opacity was calculated in each individual retrieval (392 total) from 20°N to 25°N, L_s = 90° of MY 30, nightside.

[35] Differences between the nightside and dayside distributions stem most immediately from retrieval availability, both in number and vertical range. Longitudinal sampling (Figures 5c and 5d) is better on the nightside, and dust is not retrieved to as low altitudes on the dayside as on the nightside. For example, 392 profiles are included in the nightside zonal average in this latitudinal band at L_s = 90° of MY 30 (where the dayside dust distribution is similar to that at the same season in MY 29), 374 of these profiles have reported opacity at pressure levels greater than 106 Pa, and 374 profiles have resolved local maxima in dust density-scaled opacity (see Figure 3). If characteristic retrieval spacing at this latitude is ~1.8°, there are 13 orbits per day, and 11 days in the L_s bin, we would expect ~400 retrievals in the zonal average if all retrievals were successful, so retrieval is mostly successful on the nightside. Thus, if a local maximum in dust density-scaled opacity is always present on the nightside at this latitude and season, a profile that reports opacity at a pressure level of greater than 106 Pa appears to be necessary in order to resolve it. Only 53 retrievals contribute to the zonal average on the dayside. Only two of these retrievals reported opacity at pressure greater than 106 Pa. Therefore, even if the nightside and dayside distributions were identical, the retrieved dayside profiles do not reach a pressure level/altitude sufficient to resolve the maxima observed on the nightside. In addition, the retrieved nightside profiles do not contain maxima with density-scaled opacities much greater than 10^{-3} m^2 kg^{-1}, suggesting that the available retrievals on the dayside, if they represent a diurnally invariant dust distribution, are unsuccessfully retrieved on the nightside.

[36] The diurnal variability in the pressure level/altitude at which the retrievals are cut off, retrieval availability, and the dustiness of the available retrievals appear to be connected to the latitudinal and seasonal coincidence of the HATDM with the thick water ice clouds of the seasonal (aphelion) cloud belt that covers the Martian tropics and subtropics during late northern spring and early northern summer. Just like the highest dayside zonal average dust density-scaled opacities (Figure 2d), the highest water ice column opacities on the dayside are observed between 10°S and 30°N [*Wang and Ingersoll*, 2002; *Clancy et al.*, 2003; *Smith* 2004, 2009]. Modeling [e.g., *Flasar and Goody*, 1976; *Hinson and Wilson*, 2004] and observational studies [e.g., *Tamppari et al.*, 2003; *Benson et al.*, 2003; *Möhlmann et al.*, 2009] suggest that the thickest clouds in the aphelion cloud belt are close to the surface at night, and rise along with the water vapor condensation level as temperatures warm during the day. *Heavens et al.* [2010] has recently used MCS retrievals to describe the vertical distribution of water ice during

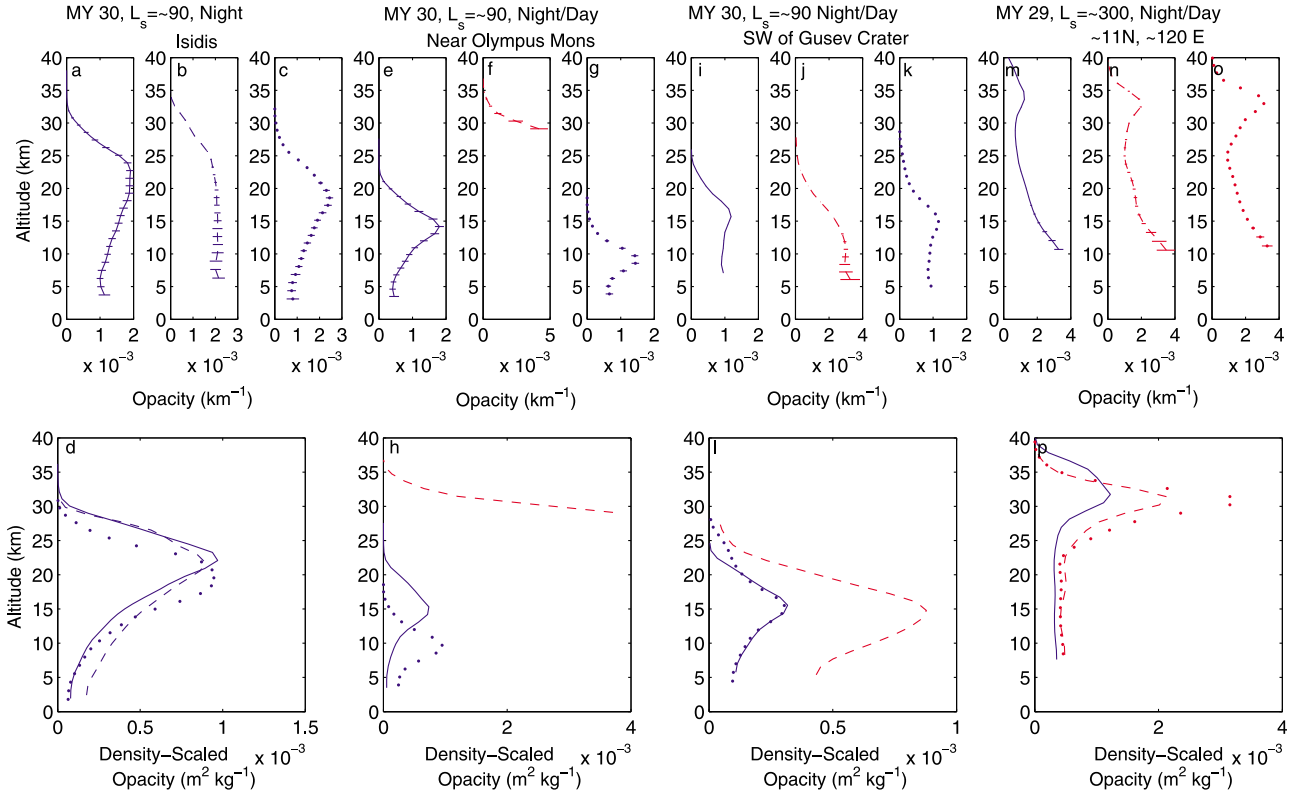

Figure 4. (top) Dust opacity (km^{-1}) and (bottom) density-scaled opacity (m^2 kg^{-1}) versus altitude above the surface for dust for individual profiles described in the text and in Table 2. Blue traces signify nightside profiles. Red traces signify dayside profiles. Profiles with solid traces are temporally prior to profiles with dashed traces, which are themselves prior to profiles with dotted traces. Solid horizontal traces on the opacity profiles plot the estimated uncertainty range of the opacity profile. If no traces are visible, the estimated uncertainty is too small to be plotted.

northern summer and identified a tropical belt of water ice clouds at 20 Pa (~35 km above the surface) at northern summer solstice. The integrated opacity of this belt is ~0.03, which would account for only ~20% of the column opacity (equivalent to A4 channel opacity) reported by *Smith* [2004, 2009].

[37] If the dayside seasonal cloud belt had a vertical extent of 25 km or less and uniform opacity vertically, the limb would be too opaque for retrieval and result in retrievals being cut off at lower pressure levels/higher altitudes on the dayside than the nightside. The dayside ascent of the seasonal cloud belt could limit dayside retrieval availability. Retrievals that are cut off at lower pressures are more likely to be rejected entirely because of large uncertainties in the pressure retrieval, since the pressure retrieval in a typical midlatitude summer profile is most sensitive to radiance measurements at 20–30 km above the surface [*Kleinböhl et al.*, 2009a].

[38] The contrast in dustiness is more difficult to explain. On one hand, dayside profiles that are dustier than average should be warmer than average and consequently less icy, so they should be preferentially retrieved on the dayside. On the other hand, there is no immediate reason why profiles like the dayside profile in Figures 4f and 4h should not be retrieved on the nightside. One possibility is that there is a process that makes the dusty profiles even more opaque at night, e.g., the thickest dust layers on the dayside nucleate nightside water ice cloud formation. Another possibility is that the profiles retrieved on the nightside reflect a dayside distribution significantly altered by sedimentation, scavenging, or some other process that acts on a diurnal timescale (see P2 for further discussion). Figures 4i–4l show a set of spatiotemporally contiguous profiles, like those plotted in Figures 4e–4h, from beyond the southern edge of the aphelion cloud belt near Gusev Crater. Individual nightside profiles with resolved maxima in dust density-scaled opacity penetrate further south at this longitude than elsewhere on the planet (see P2), so, if the dayside and nightside dust distributions are consistent, this location is one of the few places near the southern tropic where a dayside profile with a clear resolved maximum likely would be found. Indeed, all three profiles have resolved maxima, but the dayside profile's maximum is much greater in magnitude than those of the nightside profiles. Since these profiles (and those in Figures 4e–4h) are not perfectly coincident, this apparent diurnal variability still could be spatial, but if it is not, the contrast between the nightside and dayside dust distributions at this season is a genuine phenomenon, merely obscured by the observational challenges presented by the seasonal cloud belt.

[39] We also have considered the possibility that seasonal cloud belt ice particles are larger than those assumed by the MCS retrieval algorithm (3–4 μm versus 1.41 μm) [*Clancy et al.*, 2003] and the radiation scattered from the warm

Table 2. Times and Locations of the Individual Profiles Plotted in Figure 4

Figure	Line Color/Shape	MY	L_s	Local Solar Time	Date	UTC	North Latitude	East Longitude
4a, 4d	Blue solid	30	89.9276	0316	13 May 2010	0055	22	81
4b, 4d	Blue dashed	30	91.2693	0317	16 May 2010	0150	28	97
4c, 4d	Blue dotted	30	92.2005	0316	18 May 2010	0421	21	92
4e, 4h	Blue solid	30	90.2035	0314	13 May 2010	1555	15	−138
4f, 4h	Red dashed	30	90.4298	1510	14 May 2010	0413	14	−139
4g, 4h	Blue dotted	30	90.6509	0314	14 May 2010	1614	14	−133
4i, 4l	Blue solid	30	90.2753	0308	13 May 2010	1950	−16	163
4j, 4l	Red dashed	30	90.4959	1516	14 May 2010	0749	−16	170
4k, 4l	Blue dotted	30	90.7228	0308	14 May 2010	2008	−17	168
4m, 4p	Blue solid	29	297.8615	0224	5 Jul 2009	1418	12	121
4n, 4p	Red dashed	29	301.2466	1418	11 Jul 2009	0600	12	119
4o, 4p	Red dotted	29	301.8502	1417	12 Jul 2009	0618	11	124

dayside surface by the seasonal water ice clouds is interpreted as dust emission, resulting in the retrieval of spurious dust opacity. We, however, have re-retrieved dayside and nightside profiles from the northern tropics at northern summer solstice while assuming water ice particle sizes equivalent to those reported by *Clancy et al.* [2003]; the retrieved dust opacity is largely insensitive to the choice of water ice particle size.

[40] Moreover, resolved maxima in dust density-scaled opacity are a feature of zonal average and individual dust profiles in the tropics at times other than northern summer solstice. Figures 6a and 6b show resolved tropical maxima in the nightside and dayside zonal average dust distributions at L_s = 150°, a season during which the seasonal cloud belt is dissipating [*Wang and Ingersoll*, 2002]. Zonal average dust density-scaled opacity in a band centered at ~10°S is roughly a factor of 3 to 4 higher at 40 Pa than 300 Pa at L_s = 300°, MY 29 (Figures 6c and 6d). The dayside and nightside dust distributions are nearly identical. *Clancy et al.* [2003] report that dust, rather than water ice, is the dominant aerosol during this season; *Smith* [2004, 2009] observes much lower water ice column opacities at this season than at northern summer solstice; and *Wang and Ingersoll* [2002] show that visible water ice clouds at this season are confined mainly to Tharsis. Thus, occurrences of resolved maxima in density-scaled opacity can be fully decoupled from the occurrence of the aphelion cloud belt or clouds with similar characteristics.

[41] Figures 4m–4p show aerosol profiles from between Isidis and Elysium Planitiae at L_s = ~300°. All of the profiles in Figure 4g have resolved maxima in opacity as well as density-scaled opacity. One profile has a resolved maximum in density-scaled opacity of 3.5×10^{-3} m^2 kg^{-1}. In P2, a dust layer of this magnitude is attributed to outflow from a dust storm. About the time the observations from which these profiles were retrieved were made, the Mars Color Imager (MARCI) on MRO observed a dust storm in western Elysium Planitia, which moved into Isidis Planitia

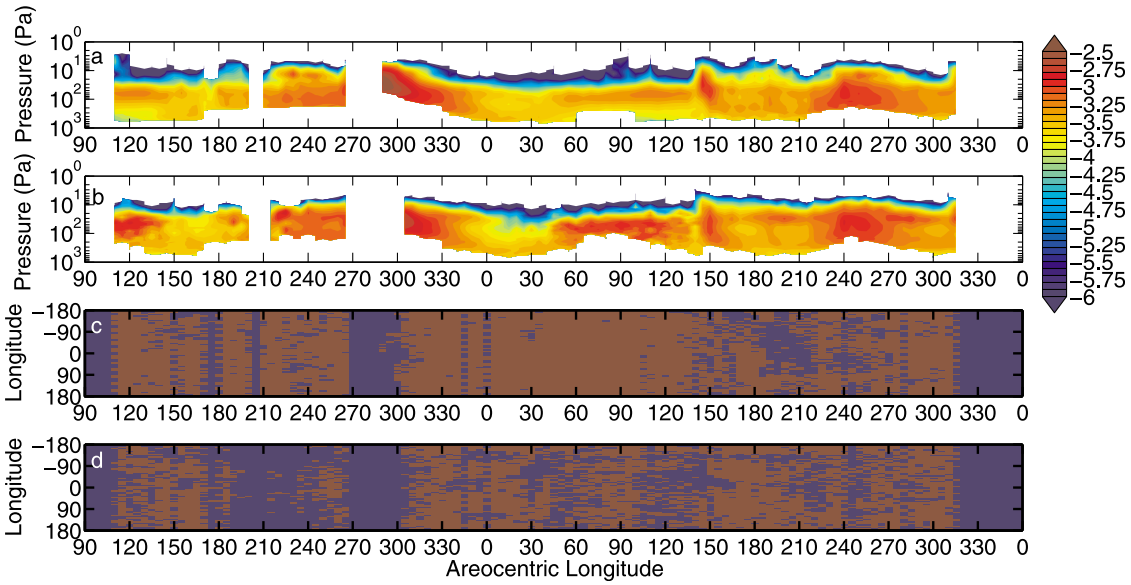

Figure 5. (a) Nightside $\log_{10}$ zonal average dust density-scaled opacity (m^2 kg^{-1}) at 20°N–25°N during MY 28 and 29. (b) Dayside $\log_{10}$ zonal average dust density-scaled opacity (m^2 kg^{-1}) at 20°N–25°N during MY 28 and 29. (c) Longitudinal sampling for Figure 5a. (d) Longitudinal sampling for Figure 5b. Red indicates there is at least one successful retrieval in the longitudinal bin, and blue indicates there are no retrievals in the longitudinal bin.

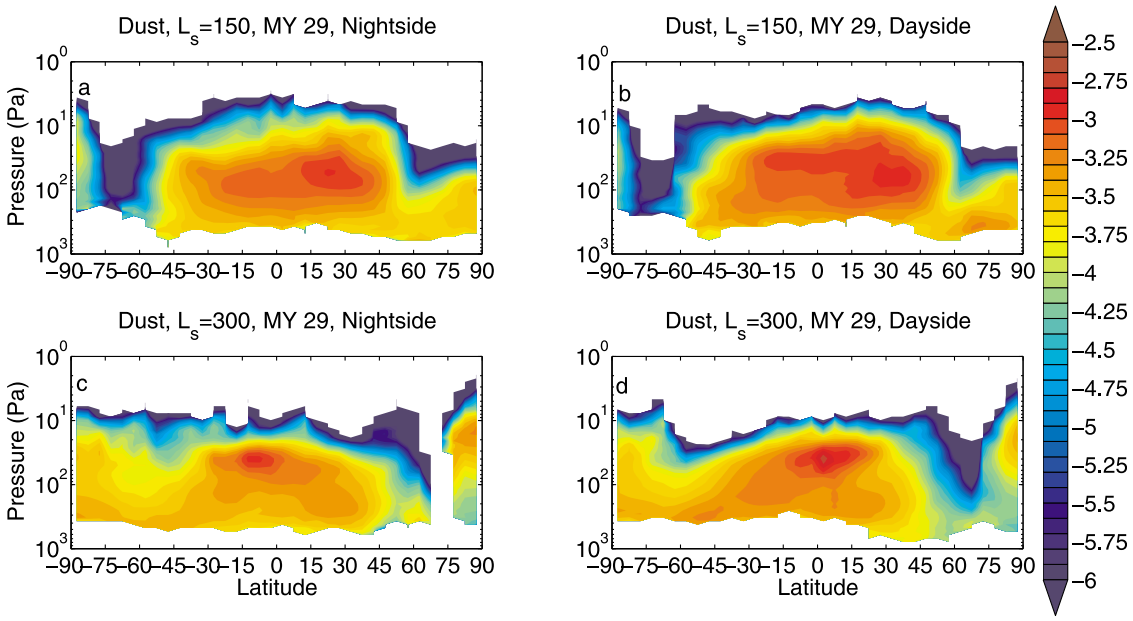

Figure 6. Log_{10} zonal average dust density-scaled opacity ($\text{m}^2\ \text{kg}^{-1}$) as labeled. Contours are every 0.1 log units. White space below the colors indicates no data. White space above the colors and the darkest blue indicates density-scaled opacity below $10^{-6}\ \text{m}^2\ \text{kg}^{-1}$.

[*Malin et al.*, 2009]. The dust layers in Figures 4m–4p could be outflow from that storm. Since the nightside profile in this case is prior in time to the dayside profiles and the resolved maxima grow with time, the contrast between the dayside profiles and the nightside profile is likely due to the advance of the dust storm toward the area.

3.3. Incompatibility of the Conrath Profile With the High-Altitude Tropical Dust Maximum

[42] A Conrath profile will not fit a resolved maximum in dust density-scaled opacity. In Figure 7a we consider a zonal average density-scaled opacity profile for the 10°–15° latitude bin in Figure 2b and rewrite equation (9) to obtain a σ-varying Conrath parameter:

$$\nu(\sigma) = \frac{\ln \frac{q}{q_0}}{1 - \sigma^{-1}} \tag{13}$$

Figure 7b shows the result of inverting the profile in Figure 7a with equation (13) by assuming a value of q_0 extrapolated from the highest σ level with density-scaled opacity information, that is, the value of q nearest the surface and thus likely closest to the value of q in the boundary layer. This inversion results in negative values of the Conrath parameter over a broad range of σ. Most fundamentally, the Conrath parameter is the ratio between the rates of sedimentation and vertical atmospheric diffusion. The model of *Conrath* [1975] accounts for the decrease of the rate of sedimentation with height due to lower atmospheric density, so variability in the Conrath parameter with respect to a vertical coordinate should be interpreted as variability in the vertical atmospheric diffusivity with that vertical coordinate. Therefore, the negative Conrath parameter region in Figure 4b is presumably one with negative vertical atmospheric diffusivity. In the Conrath model, unphysical diffusion from regions of lower concentration to those of higher concentration would be necessary to account for the observed variability.

[43] Figure 7c shows the profile in Figure 7a inverted with equation (13) by assuming a value of q_0 equivalent to the density-scaled opacity maximum in the profile. In this case, the Conrath parameter increases toward higher σ (or lower altitude), which could be interpreted to mean that vertical diffusion weakens closer to the surface of Mars, precisely the region of the atmosphere in which vertical diffusion should be most vigorous due to turbulent interactions between the atmosphere and the surface. Inferring a much higher value for q_0 than the maximum in the density-scaled opacity also results in the Conrath parameter increasing and atmospheric diffusivity decreasing toward the surface. Therefore, the presence of a maximum in mass mixing ratio that is not at the surface is inconsistent with the assumptions underlying the Conrath profile and motivates an alternate method for compactly representing the vertical dust distribution.

3.4. An Alternative Representation Scheme

[44] We have developed an alternative to the Conrath profile to represent the seasonal variability in the vertical dust distribution. While this scheme was not intended for immediate application to aerosol prescription in Martian atmospheric models, our general approach could be foundational for such efforts. Figure 8 shows two examples of end-member profiles, which have been created from zonal averages of individual density-scaled opacity profiles interpolated on a sigma grid between 10^{-3} and 1, thus averaging each profile on a grid with a common local surface. One profile has a significant local maximum in density-scaled opacity (Figure 8a) and one lacks such a maximum (Figure 8b). The profile in Figure 8b could be represented by a Conrath profile. Inversion with equation (13) suggests that it

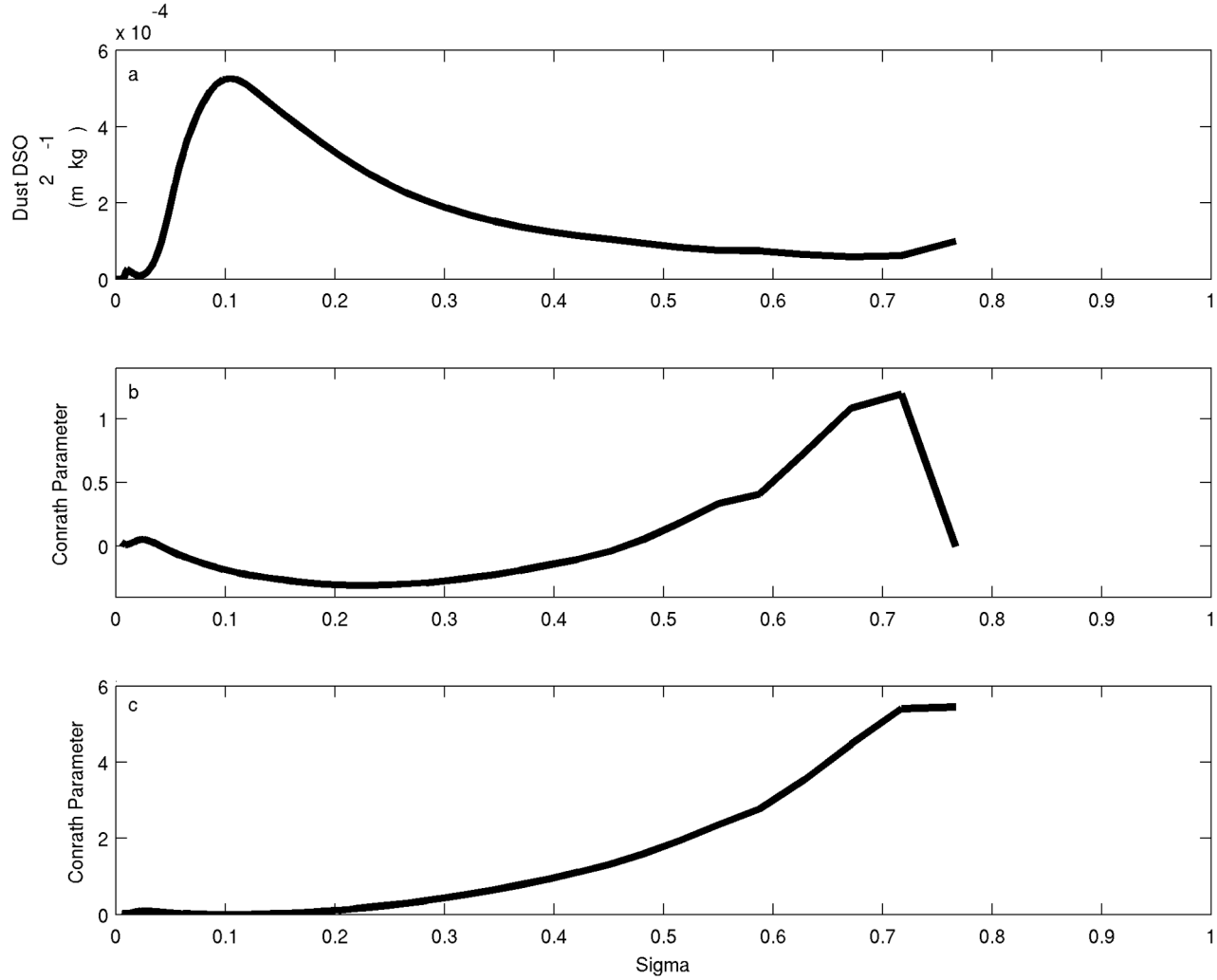

Figure 7. (a) Zonal average of the density-scaled opacity (m^2 kg^{-1}) interpolated onto σ coordinates for nightside retrievals, L_s = 90, MY 30, 10°N–15°N. (b) Inferred Conrath parameter, $\nu(\sigma)$ for the profile in Figure 7a, assuming $q_0 = 1.00 \times 10^{-4}$ m^2 kg^{-1}. (c) Inferred Conrath parameter, $\nu(\sigma)$ for the profile in Figure 7a, assuming $q_0 = 5.27 \times 10^{-4}$ m^2 kg^{-1}.

would be a Conrath profile with an exponentially increasing Conrath parameter with height (or vertical diffusivity exponentially decreasing with height). Such a diffusivity profile is physically plausible. The dust profile in Figure 8a cannot be represented by a Conrath-like profile, but it could be represented by a superposition of a profile like the one in Figure 8b and of an additional component to represent an enriched layer. By trial and error, we found that the profile in Figure 8b could be represented by a function of the form

$$\frac{d_z\tau}{\rho} = \left(\frac{d_z\tau}{\rho}\right)_0 \Xi(\ln\sigma - \ln\sigma_0)\left\{1 - \exp\left[\frac{-(\ln\sigma - \ln\sigma_0)^2}{m_0^2}\right]\right\} \tag{14}$$

where $(d_z\tau/\rho)_0$ is the near-surface density-scaled opacity, that is, the density-scaled opacity in the portion of the profile with approximately uniform density-scaled opacity; Ξ is the Heaviside function, and σ_0 and m_0 are parameters with physical significance that shall be demonstrated. Figure 8b shows a fit of the profile using equation (14) and the fitting procedure described in section 3.5. It does not fit a small feature near the surface but otherwise captures the general form of the profile.

[45] The function used in equation (14) is a Gaussian. Its success in this context should not be interpreted to have any physical significance. The retrieval algorithm uses Gaussian smoothing in the forward modeling process, so retrieved features tend to take the form of Gaussians. By trial and error, it was found that an additional Gaussian would represent the enriched layer in Figure 8a, such that the functional form would be

$$\frac{d_z\tau}{\rho} = \left(\frac{d_z\tau}{\rho}\right)_0 \left(\Xi(\ln\sigma - \ln\sigma_0)\left\{1 - \exp\left[\frac{-(\ln\sigma - \ln\sigma_0)^2}{m_0^2}\right]\right\} + B\exp\left[\frac{-(\ln\sigma - \ln\sigma_1)^2}{m_1^2}\right]\right) \tag{15}$$

where B, m_1, and σ_1 are additional parameters.

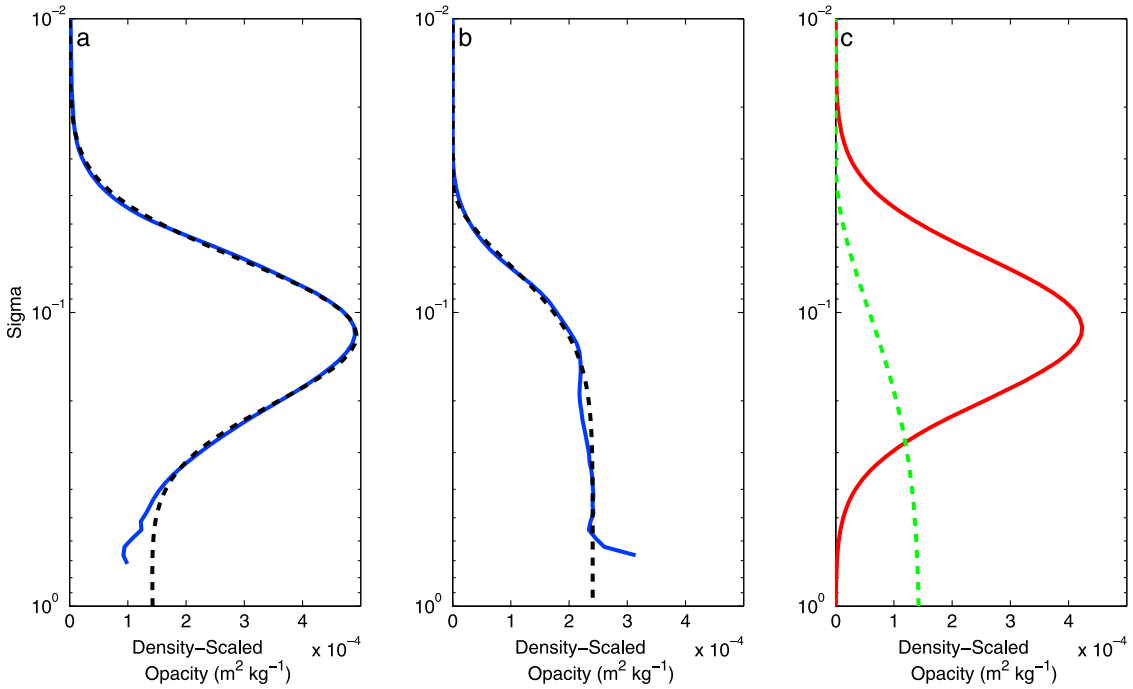

Figure 8. (a) Zonal average of the density-scaled opacity (m^2 kg^{-1}) interpolated onto σ coordinates for nightside retrievals, L_s = 90, MY 30, 20°N–25°N (blue solid line) plotted with fit by equation (15) (black dashed line). (b) Same as Figure 8a, except for L_s = 90, MY 30, 60°N–65°N. (c) Decomposition of the fit in Figure 8a into Conrath-like component (green dashed line) and layer component (red solid line).

[46] Figure 8a shows a fit of equation (15) to the profile. Figure 8c shows the decomposition of the fit in Figure 8a to its Conrath-like (equation (14)) and layer-like (difference of equation (15) and equation (14)) components. An interesting result is that the decrease in mass mixing ratio at low σ appears to occur at a higher σ level in the profile in Figure 8a than in the profile in Figure 8b. The principal result, however, is that these two end-member profiles both can be described by equation (15), though B = 0 (and σ_1 and m_1 will be undefined) for the profile in Figure 8b.

[47] The decomposition in Figure 8c also provides insight into the significance of the parameters in equation (15), all of which can be estimated from the component curves of the fit as annotated in Figure 9. First, one feature of the profile is its "near-surface dustiness" (NSD), the characteristic density-scaled opacity/mass mixing ratio near the surface:

$$\mathrm{NSD} = \left(\frac{d_z\tau_1}{\rho_0}\right)_0 \tag{16}$$

Second, equation (16) can be weighted by B to recover the characteristic density-scaled opacity corresponding to the dust mass-mixing ratio in the principal local maximum in the profile, the "perturbation" or "pulse dustiness" (PD):

$$\mathrm{PD} = B\left(\frac{d_z\tau_1}{\rho_0}\right)_0 \tag{17}$$

Note that since the falloff from constant mass mixing ratio generally occurs above this maximum, the true maximum in mass mixing ratio usually is proportional to the sum of near-surface dustiness and pulse dustiness.

[48] There is a characteristic altitude above the surface at which the mass mixing ratio falls off to effectively zero, the falloff height (FH). The falloff height is the top of the dust haze, at least to the extent measurable by the retrievals. There is also an altitude at which the peak of the "pulse" occurs, "the pulse height" (PH). These parameters can be defined as

$$\begin{aligned}\mathrm{FH} &= -H\ln\sigma_0\\ \mathrm{PH} &= -H\ln\sigma_1\end{aligned} \tag{18}$$

[49] Finally, the characteristic length scale on which density-scaled opacity decays from near-surface dustiness to 0 is the falloff length (FL), and the characteristic length scale of the "pulse," the "pulse thickness" (PT), can be defined as

$$\begin{aligned}\mathrm{FL} &= m_0 H\\ \mathrm{PT} &= m_1 H\end{aligned} \tag{19}$$

An alternative approach to defining the thickness of the pulse would be to consider its full width at half maximum, which should be ~1.66 PT.

3.5. Fitting Profiles Using the Scheme

[50] The profiles in Figures 8a and 8b (and the other zonal average density-scaled opacity profiles from northern spring and summer) were fit in several steps. First, the zonal average density-scaled distributions were filtered to exclude two sources of aerosol opacity retrieved as dust opacity that is likely not dust opacity. Opacity near the winter pole (Figures 2a, 2b, 2d, and 6a–6d) is thought to be CO_2 ice

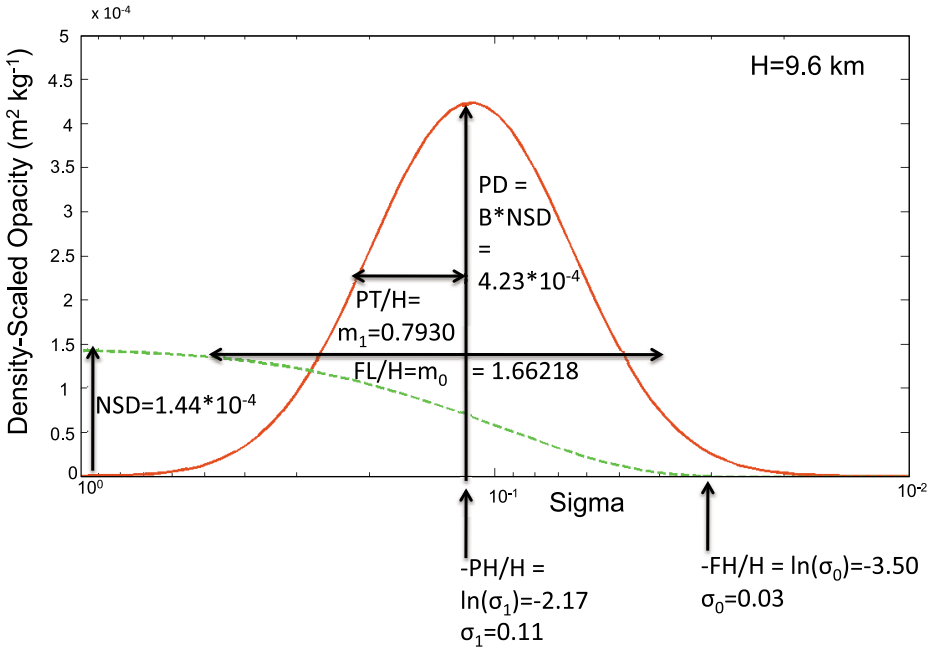

Figure 9. Annotated diagram of the fit in Figures 8a and 8c, showing the relationship between parameters of equation (15) and more physically meaningful parameters. Annotations of a particular arrow are always below or to the right of the corresponding arrow. The lengths of FL and PT are approximate.

[*Kleinböhl et al.*, 2009a; *McCleese et al.*, 2010; *Hayne*, 2010]. Opacity is not reported in MCS retrieved profiles delivered to the Planetary Data System (PDS) if the temperature is less than 10 K above the CO_2 frost point. A similar filter is applied here. Apparent detached dust hazes with density-scaled opacities of ~10^{-4} m^2 kg^{-1} at pressure levels of less than 10 Pa over the tropics that are seen on the nightside but not the dayside (Figures 2b and 2d) are due to maxima at pressures < 10 Pa in dust opacity and density-scaled opacity in ~1% of retrieved profiles from this latitude, time of day, and season. The maxima in density-scaled opacity in these hazes are up to ~10^{-2} m^2 kg^{-1}, which is higher than density-scaled opacities observed during the 2007 global dust storm. These profiles are associated with characteristic structures in the MCS radiance measurements, which are thought to be signatures of previously reported mesospheric clouds of carbon dioxide ice and/or water ice [e.g., *Montmessin et al.*, 2006, 2007; *Clancy et al.*, 2007; *McConnochie et al.*, 2010]. These features are filtered out of the observations by identifying zonal average profiles with a second maximum in density-scaled opacity at a sigma level less than 0.0386 (chosen to distinguish the HATDM and these features), finding the minimum value of density-scaled opacity between the maxima, and setting to zero all density-scaled opacity at lower sigma levels than this minimum. Density-scaled opacity at latitudes and sigma levels with opacity less than 10^{-5} km^{-1} then was set to zero.

[51] Second, $(d_z\tau_1/\rho_0)_0$ was diagnosed by estimating the σ level at ~8 km from the surface by using a value of H estimated from the zonal average temperature on all pressure levels with data between 100 and 1000 Pa. The profile then was scaled by the diagnosed $(d_z\tau_1/\rho_0)_0$. In some cases, data is available at higher σ levels, but the retrievals contributing to the average sample from a much smaller number of longitudes, suggesting that a few retrievals with unusually low LOS opacity in dust (or ice) may be contributing to the average. Therefore, diagnosing $(d_z\tau_1/\rho_0)_0$ at the highest σ level with data might bias the estimate to atypical conditions. If the estimated σ level at ~8 km from the surface has no data, diagnosis is attempted at a sigma level that is a half scale height higher. If this level has no data, the profile is not fit. These flexible criteria allow the fitting scheme to be used in almost all areas with available retrievals in northern spring and summer, particularly in late northern summer near the north pole, where low-level water ice clouds normally limit the vertical range of retrievals to 12–13 km. Due to this method of diagnosis, the resolved maxima either can be accentuated or diminished relative to the lower region of assumed uniform mixing.

[52] Third, MATLAB multivariable nonlinear fitting algorithms were used to fit the scaled profile with likewise scaled versions of equations (14) and (15). Ideally, equation (15) would fit a profile such as the one in Figure 8b with B = 0. In practice, curvefitting algorithms seek to minimize variance between the data and the fit curve and will introduce the second Gaussian to do so. Such Gaussians typically have implausible values of m (equivalent to PT > 100 km). In other words, equation (15) may overfit the data, which is a common occurrence in fitting curves. Therefore, the equation (14) and (15) fits were evaluated by an F ratio test using the residual sum of squares from each fit ($RSS_{14,15}$), where F is defined as

$$F = \frac{\dfrac{RSS_{14} - RSS_{15}}{RSS_{14}}}{\dfrac{p_{15} - p_{14}}{n - p_{15}}} \tag{20}$$

and where p_{14} and p_{15} are the number of free parameters in the scaled versions of equations (14) and (15). Note that $p_{16} = 5$ and $p_{15} = 2$, respectively, and n is the number of degrees of freedom in the data. Ideally, this ratio tests the null hypothesis that equation (15) is a better fit to the data than equation (16) by comparison with an F distribution with parameters p_{15}–p_{14} and n-p_{15}.

[53] The number of degrees of freedom in the data, however, is not simply the number of data points in the fit profile. The fit profile is an average of individual profiles with a vertical resolution of ~5 km interpolated successively onto two grids. The first grid (the pressure grid) was ~5 times finer than the original resolution, while the second grid (the σ grid) is ~1.6 times finer than the resolution of the pressure grid. From the definition of RSS

$$\mathrm{RSS} = \sum_{i=1}^{N} [y_i - f(x_i)]^2 \tag{21}$$

RSS of the same data, y_i and fitting function, $f(x_i)$, will scale in proportion to the square of the number of data points, N. So if the same data is interpolated onto a uniformly finer grid, RSS is should increase in proportion to N^2. Provided the interpolations onto the pressure and sigma grids were uniform (they were approximately so), this factor will cancel in equation (20), so F will be the same for the interpolated grids and a grid with data points equivalent to the intrinsic degrees of freedom. We estimate that n should be approximately equal to 5 for an individual dust opacity retrieval, since ~5 detectors in the A5 channel of MCS are used to retrieve dust. However, A5 radiances are dependent on the temperature profile as well, so the ~8 detectors in channels A1, A2, and A3 observe the same part of the limb as the A5 detectors to retrieve temperature, thereby providing some implicit constraint on dust. For the fits presented in this paper, n is conservatively assumed to be 10. The critical value of the F ratio for the 95% confidence interval for n = 10 is 5.4095, which was used to determine whether the fit using equation (14) or the fit using equation (15) should be used. To limit bias by the near-surface dust and the assumption of zero values near the top of the domain, the fit was limited to the domain between where $(d_z\tau_1/\rho_0)_0$ was diagnosed and where the zonal average dust opacity had fallen to 0.1% of its near-surface value.

[54] The R^2 values for the fits during northern spring and summer are normally very good (>0.9) (Figures 10a–10d). The exceptions mainly are at latitudes and time of year where profiles with and without local maxima are present in roughly equal proportions.

4. Results and Discussion

4.1. Results

[55] Over most of the planet, near-surface dustiness is greater at the equinoxes than at northern summer solstice (Figure 11). At northern summer solstice, near-surface dustiness approximately increases toward the north pole, particularly since the atmosphere is effectively clear of dust south of 45°S (at least at those latitudes where CO_2 ice is likely absent). The dust-clear region in the southern extratropics appears to follow the noon terminator and extends up to 20° north of it. The area around the north pole becomes clear of dust in late northern summer of MY 28 and MY 29. Values of pulse dustiness comparable to or greater than near-surface dustiness are mainly restricted to the tropics; they are sometimes seen near the north pole (Figure 12).

[56] The variability during northern spring and summer of MY 28 and 29 in falloff height, falloff length, pulse height, and pulse thickness are plotted in Figures 13–16. The dominant variability in these parameters primarily occurs in the tropics and will be discussed in concert with variability in near-surface dustiness and pulse dustiness in section 4.2.

4.2. The Tropical Dust Distribution

[57] From $L_s = 110°$ to 160° of MY 28 and from $L_s = 45°$ to 140° of MY 29, the tropical dust distribution has a well-defined character, which is seen most easily in the analysis of the nightside retrievals. The lower end of MCS's vertical range is clearer of dust than at the equinoxes (Figures 11a and 11b). At ~25 km above the surface of the northern tropics, dust concentrations are enriched by a factor of 2 to 10 relative to the lower end of MCS's range. A generally weaker enrichment is seen in the southern tropics at ~15 km above the surface (Figures 12a, 12b, 14a, and 14b). Therefore, the HATDM seen in Figures 2a and 2b and its greater northern magnitude and intensity are persistent features of the planetary vertical dust distribution for roughly a quarter of the Martian year.

[58] Previously published observations that could corroborate the existence of this feature usually lack the ability to discriminate between dust and water ice, and/or an aerosol layer where both are present. A good example is from *Jaquin et al.* [1986, p. 442], who analyzed solar reflectance profiles derived from Viking limb imagery in the northern subtropics during late northern spring and early northern summer and found "a series of layers in the extinction profile between 4 and 10 km in width…" Jaquin et al. found similar layers centered at ~14 and ~37 km in the aerosol structure of the southern subtropics during the same season. As discussed in section 3.2, the lower altitude layers probably were composed of both dust and water ice, while the higher altitude layer probably was composed of water ice alone (neglecting any dust nuclei).

[59] The relative stability of the tropical dust distribution during middle to late spring and early summer makes the changes in the dust distribution at these latitudes in middle to late northern summer all the more striking. In MY 28, the alteration in the dust distribution is relatively gradual; the primary change that can be seen before the period of limb staring is a decrease in the latitudinal extent of the pulse and an increase in near-surface dustiness (Figures 11a and 12a). In MY 29, near-surface dustiness and pulse dustiness both increase throughout the tropics and into the northern and southern midlatitudes (Figures 11b, 11d, 12b, and 12d) at around $L_s = 135°$, slightly earlier in the season than MY 28. But the vertical extent of the dust is the more crucial difference between the dust distributions of these years. Pulse height and pulse thickness increase to 30–40 km and 10–15 km, respectively, at $L_s = 145°$ (Figures 14b, 14d, 16b, and 16d), while falloff height increases to as high as 60 km for the remainder of northern summer (Figures 13b and 13d).

[60] Differences between MY 28 and MY 29 in the seasonal evolution and character of the dust distribution during

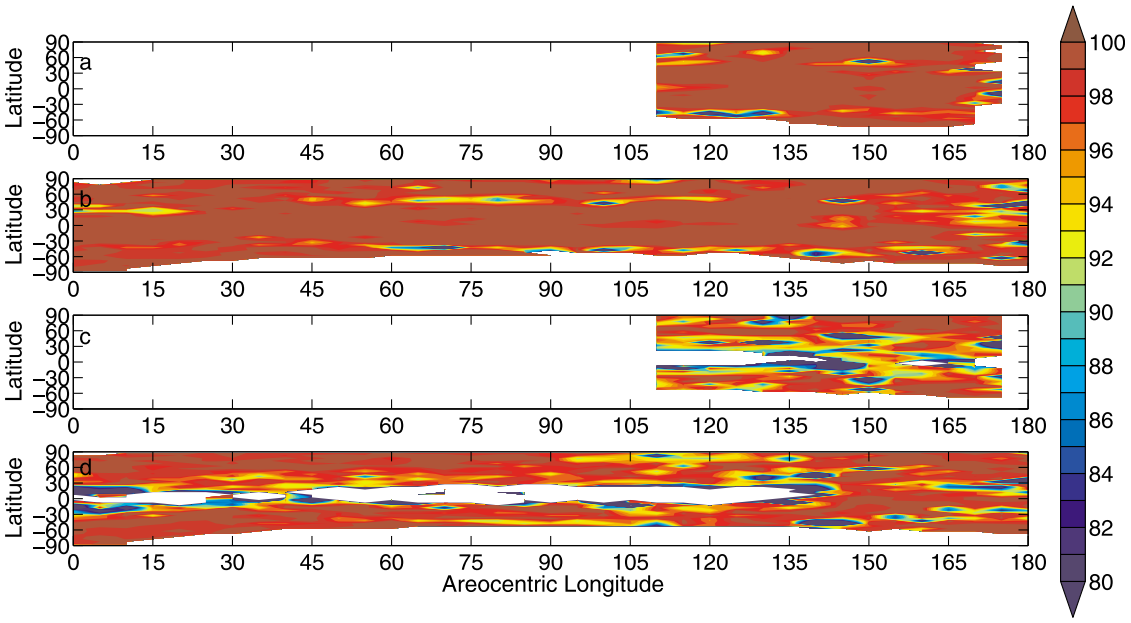

Figure 10. Latitudinal and seasonal variability in R^2 of the fits of the zonal average density-scaled opacity profiles: (a) MY 28, nightside; (b) MY 29, nightside; (c) MY 28, dayside; (d) MY 29, dayside.

late summer are likely due to greater "early season" tropical dust storm activity [*Malin et al.*, 2008; *Smith*, 2009] observed by MARCI and THEMIS, which may most strikingly manifest itself in an aspect of the distribution not as easily observed by these instruments: layering within the dust distribution. Dustier conditions near the surface observed by MARCI and THEMIS also could explain the earlier and greater degradation in longitudinal sampling and marginally higher values of near-surface dustiness in the northern tropics and midlatitudes during this season (Figures 1a, 1b, and 12a–12d) in MY 29. (Note that in late summer of MY 28, MCS was experiencing some technical

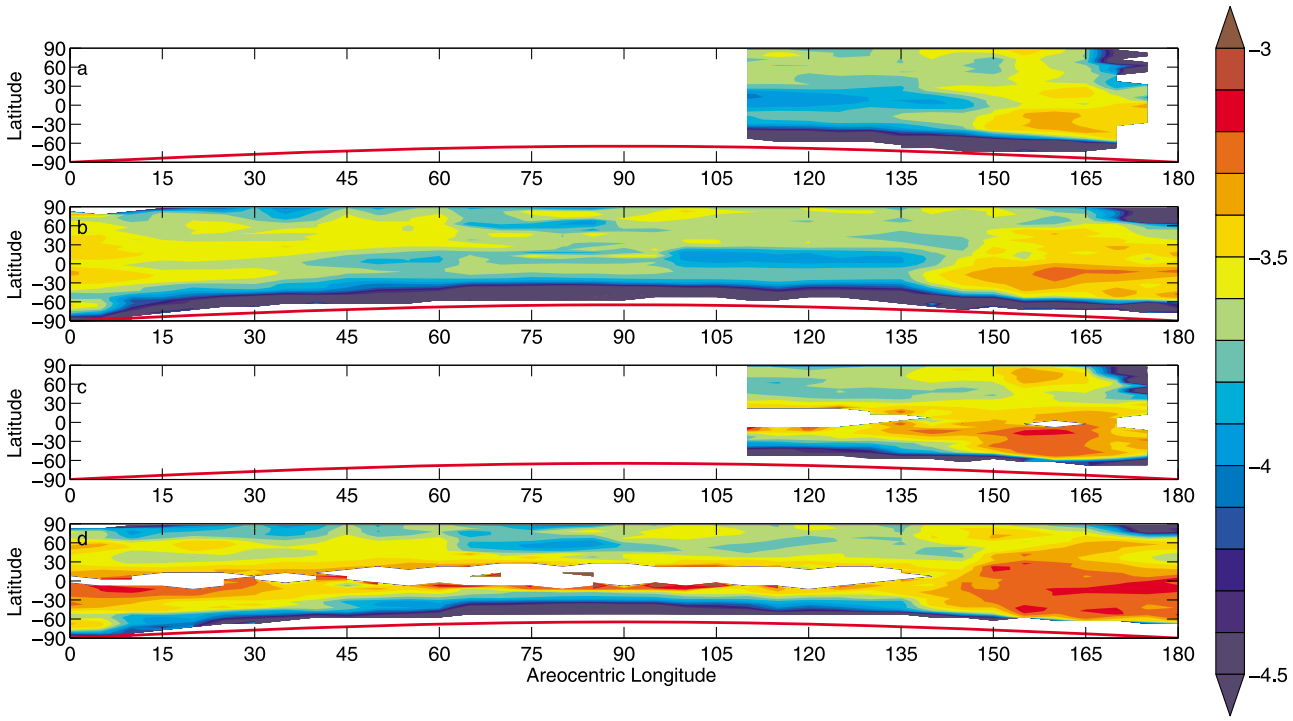

Figure 11. Latitudinal and seasonal variability in $\log_{10}$ (near-surface dustiness), ($m^2\ kg^{-1}$) during northern spring and summer. The red line marks the northern edge of southern polar night: (a) MY 28, nightside; (b) MY 29, nightside; (c) MY 28, dayside; (d) MY 29, dayside. White space is missing data. The deepest blue represents near-surface dustiness $<10^{-6}$ $m^2\ kg^{-1}$ or effectively dust-free areas.

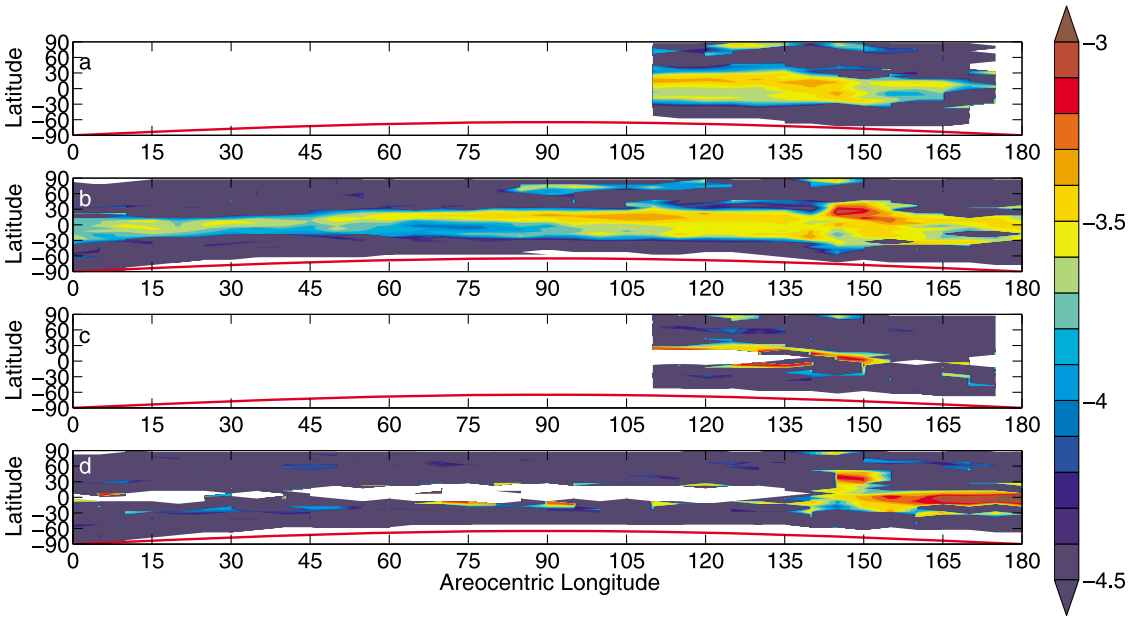

Figure 12. Latitudinal and seasonal variability in $\log_{10}$ (pulse dustiness), (m^2 kg^{-1}) during northern spring and summer. The red line marks the northern edge of southern polar night. (a) MY 28, nightside; (b) MY 29, nightside; (c) MY 28, dayside; (d) MY 29, dayside. White space is missing data. The deepest blue represents pulse dustiness $<10^{-6}$ m^2 kg^{-1}.

issues, which resulted in data collection gaps, so the sampling contrast due to retrieval success between MY 29 and MY 28 is not as readily captured by Figures 1a and 1b as it could be.)

[61] During late summer of MY 29, the zonal average dayside maximum in dust density-scaled opacity in the tropics tends to be greater in magnitude, thinner, and higher in the atmosphere than the nightside (Figures 12b, 12d, 14b, 14d, 15b, 15d, 16b, and 16d). The dayside and nightside

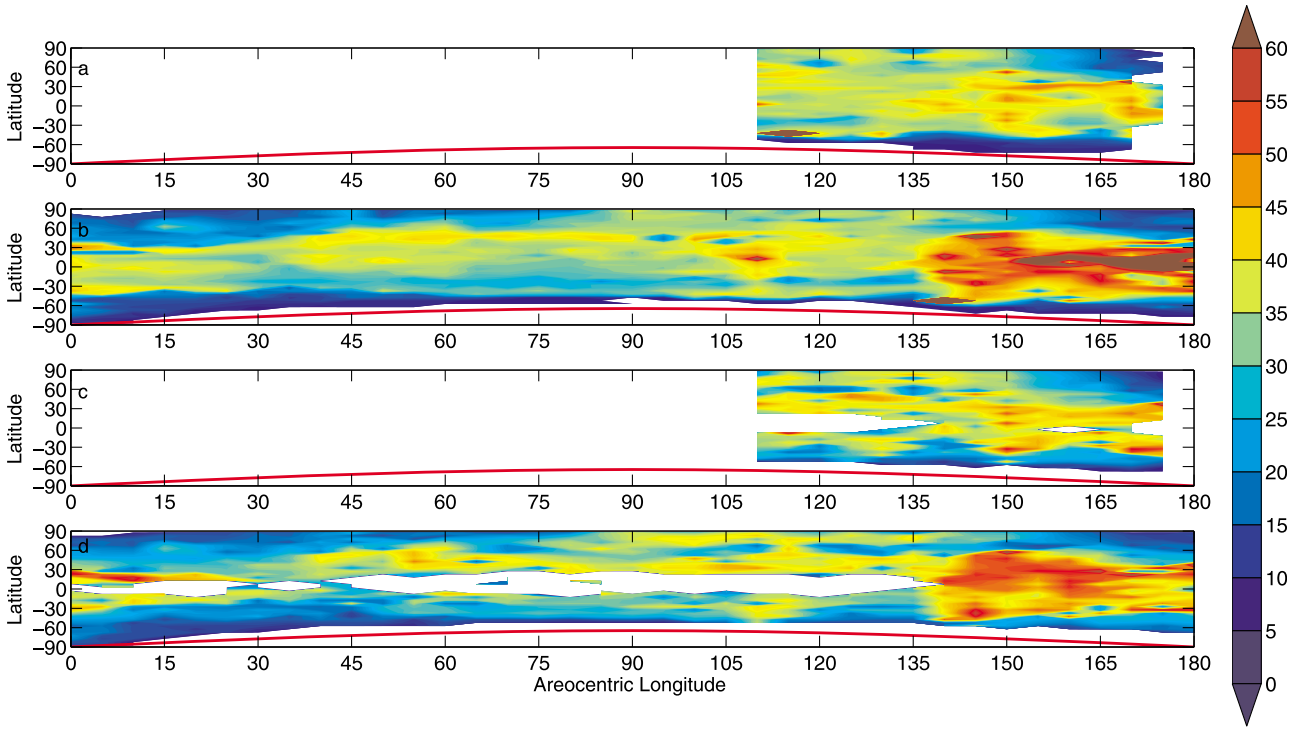

Figure 13. Latitudinal and seasonal variability in falloff height (km) during northern spring and summer. (a) MY 28, nightside; (b) MY 29, nightside; (c) MY 28, dayside; (d) MY 29, dayside. The red line marks the northern edge of southern polar night.

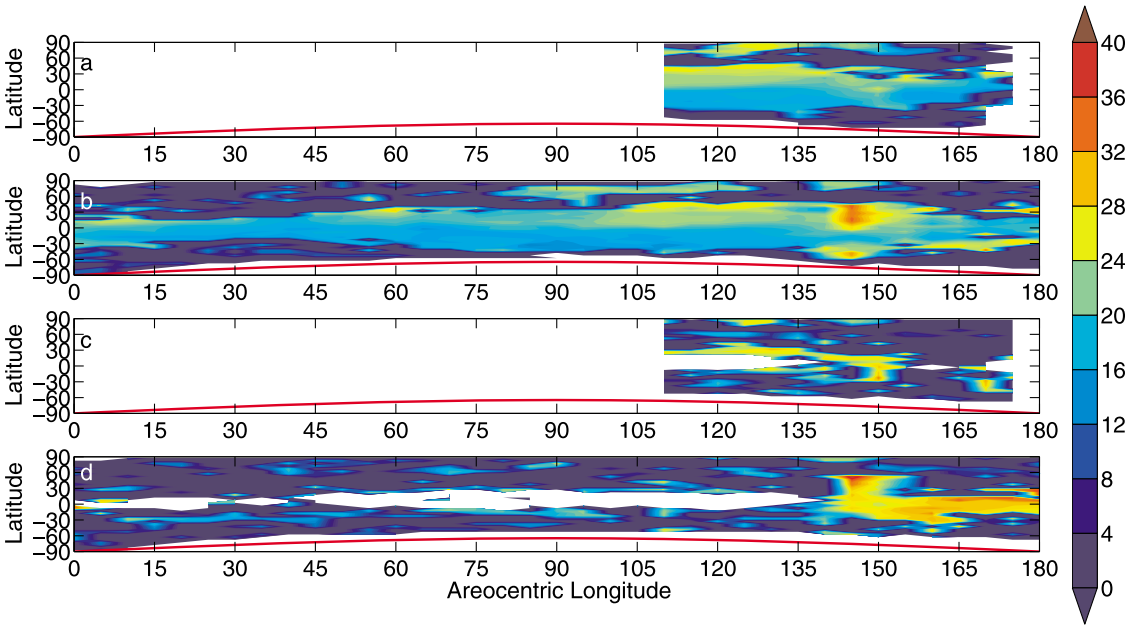

Figure 14. Latitudinal and seasonal variability in pulse height (km) during northern spring and summer. (a) MY 28, nightside; (b) MY 29, nightside; (c) MY 28, dayside; (d) MY 29, dayside. The red line marks the northern edge of southern polar night.

distributions are very similar at $L_s = 145°$ but diverge thereafter. The contrast between the zonal average distributions reflects strong diurnal variability in the dust distribution in some, but not all, parts of the tropics. Figures 17a–17c show a dayside dust profile compared with a nightside profile 12 h later (see Table 3). The locations of the profiles are coincident at the horizontal resolution of MCS, but the profiles themselves are radically different. The dayside profile has a vertically narrow local maximum in dust density-scaled opacity of ~2.4×10^{-3} m^2 kg^{-1} at ~30 km above the surface. This feature has eroded so much 12 h later that the profile appears nearly uniform. Similar diurnal variability is illustrated by the set of profiles in Figures 17d–17g, in which the local maximum in the profile on the dayside is higher in the atmosphere and higher in magnitude than those in the nightside profiles at nearby locations.

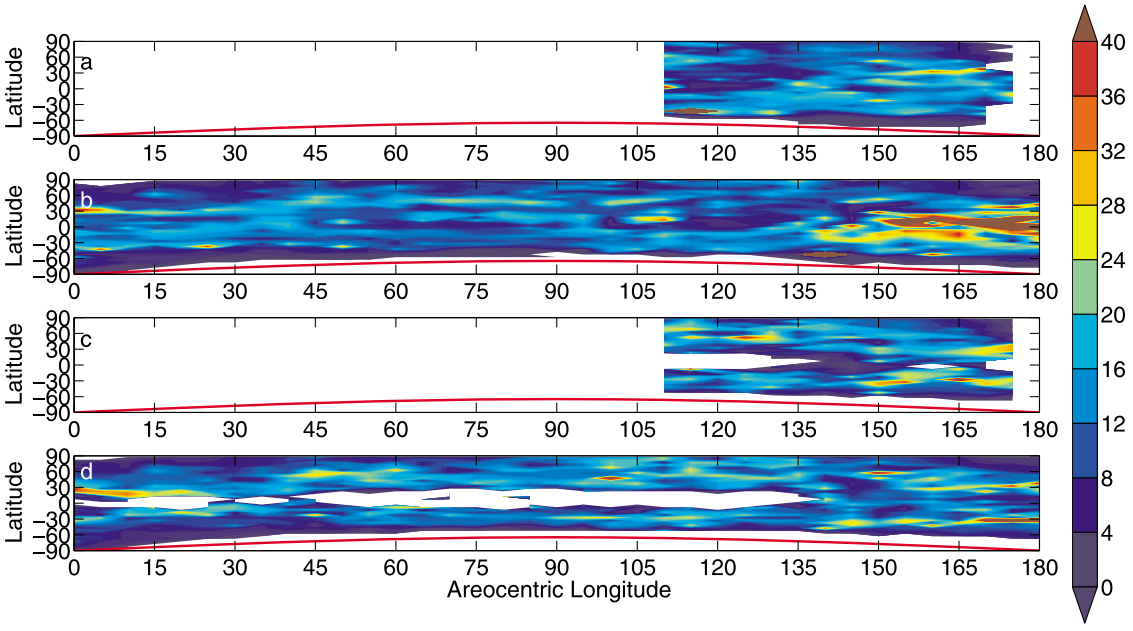

Figure 15. Latitudinal and seasonal variability in falloff length (km) during northern spring and summer. (a) MY 28, nightside; (b) MY 29, nightside; (c) MY 28, dayside; (d) MY 29, dayside. The red line marks the northern edge of southern polar night.

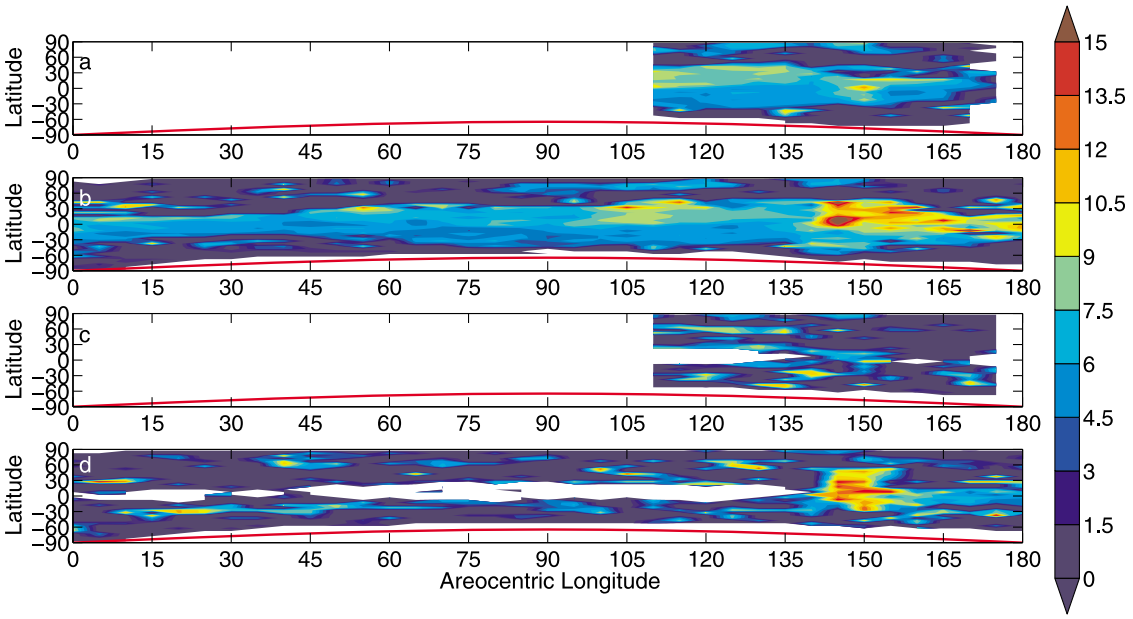

Figure 16. Latitudinal and seasonal variability in pulse thickness (km) during northern spring and summer. (a) MY 28, nightside; (b) MY 29, nightside; (c) MY 28, dayside; (d) MY 29, dayside. The red line marks the northern edge of southern polar night.

Elsewhere in the tropics, diurnal variability is weaker in a set of profiles with multiple maxima also retrieved from observations 12 h apart (Figures 17h–17k). Figures 17l–17o possibly show of the evolution of the dust distribution near Huygens Crater over the course of 36 h as opacity at ~10 km above the local surface drops below the LOS opacity limit to reveal a resolved maximum in dust density-scaled opacity. In P2, it is shown that the HATDM at northern summer solstice on the nightside consists of coherent layers over two broad longitudinal ranges, though its diurnal variability is more uncertain. The tropical dust distribution during late summer of MY 29 appears to have more complex diurnal variability and longitudinal heterogeneity.

4.3. Radiative-Dynamical Significance of the High-Altitude Tropical Dust Maximum

[62] The HATDM in late northern spring and early northern summer and the analogous feature of higher magnitude and altitude during middle to late northern summer of MY 29 are of great dynamical interest, because they would produce a different radiative heating profile in the atmosphere than typically assumed by models. Diabatic heating and cooling rates due to an aerosol are directly linked to its density-scaled opacity or mass mixing ratio. A high-altitude dust maximum makes the vertical dust distribution of the atmosphere "top heavy," so that the strongest dust heating/cooling is well above the surface. Since the mass mixing ratio at 20 km contributes much less to the column opacity than the mass mixing ratio near the surface, a "top heavy" mass mixing ratio profile creates a higher rate of diabatic heating/cooling at ~20 km in Mars's atmosphere than uniformly mixed dust, even for relatively low column opacities. Since atmospheric models generally assume uniformly mixed dust to some height or decreasing mass mixing ratio with height profiles ("bottom heavy" profiles), incorporating an equatorial dust pulse might produce a radiative heating profile due to dust with a similar elevated maximum. The heating profile in the Earth's tropics is similarly perturbed by the release of latent heating by moist convection, which tends to peak 5 to 10 km above the surface [*Tao et al.*, 2001].

[63] The visible heating rate, J, can be estimated as

$$J = 7.3\varepsilon \frac{d_z \tau}{\rho} F_{in} \tag{22}$$

where 7.3 is the ratio between visible opacity and MCS A5 opacity, ε is the efficiency of absorption of solar radiation in the visible, and F_{in} is the incident solar radiation. Typical tropical near-surface dustiness is 2.5×10^{-4} m^2 kg^{-1}, F_{in} at noon at the subsolar point on Mars is ~500 W m^{-2}, and ε is minimally the additive inverse of the single scattering albedo, 0.05–0.1 and possibly somewhat higher. The heating rate will be ~4.5×10^{-2}–9.0×10^{-2} W kg^{-1} or 5.3–10.6 K sol^{-1}. Typical tropical pulse dustiness is a factor of 0.5 to 3 higher, producing zonally averaged heating rates within the pulse as large as ~30 K sol^{-1} if skies above the dust haze are clear. Due to the relatively deep mixing of dust at these latitudes, the effective heating rate will be proportional to the sum of near-surface dustiness and pulse dustiness. Heating rates in the HATDM in middle to late northern summer of MY 29 may have been up to 3 times as great.

[64] Visible heating of dust will not be much affected by the water ice cloud deck at 20 Pa (and at lower pressures in late northern summer) reported by *Heavens et al.* [2010]; its zonal average visible optical depth is no more than ~0.07. Shortwave heating will be more greatly affected by the dayside aphelion cloud belt, which we suggest in section 3.2 may have a vertical range very similar to that of the dust maximum. The aphelion cloud belt's zonal average visible optical depth is ~0.45. If the cloud belt is mostly above the dust maximum, some incoming solar radiation will be

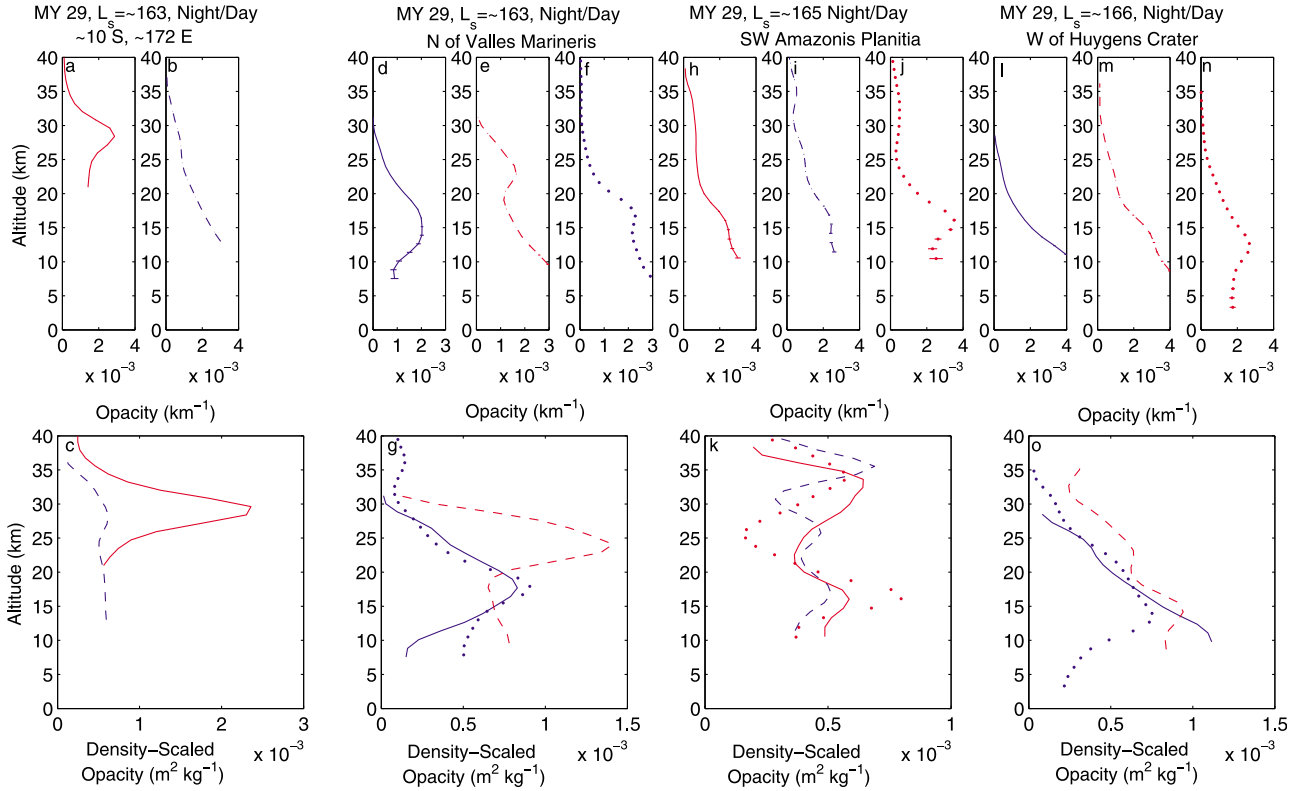

Figure 17. (top) Dust opacity (km^{-1}) and (bottom) density-scaled opacity (m^2 kg^{-1}) versus altitude above the surface for dust for individual profiles described in the text and in Table 3. Blue traces signify nightside profiles. Red traces signify dayside profiles. Profiles with solid traces are temporally prior to profiles with dashed traces, which are themselves prior to profiles with dotted traces. Solid horizontal traces on the opacity profiles plot the estimated uncertainty range of the opacity profile. If no traces are visible, the estimated uncertainty is too small to be plotted.

reflected back to space before interacting with the dust. If the opposite is true, the dust will interact with both incoming sunlight and reflected sunlight from the cloud belt rather than reflected sunlight from the more highly absorbing Martian surface. It is also possible that water vapor could condense on dust particles within the dust maximum, raising the single scattering albedo of the dust particles to near unity and limiting their visible heating effect.

[65] The dust also will have an infrared heating and cooling effect, depending on the thermal structure of the atmosphere. During the day, lapse rates are strongly negative over the tropics, so that dust will tend to re-emit infrared radiation absorbed from the strongly heated surface at a somewhat lower temperature than the surface, producing net heating. In a more top heavy dust distribution, there are higher concentrations of dust higher on the atmosphere (and therefore at a cooler temperature) relative to a uniformly mixed profile, so infrared heating, too, will be greater. At night, there is an inversion within 2 km of the surface [*Gierasch and Goody*, 1968], so the surface emits at fairly cool temperatures and any aerosol above the inversion (up to ~10 Pa) may re-emit at a higher temperature than the

Table 3. Times and Locations of the Individual Profiles Plotted in Figure 17

Figure	Line Color/Shape	MY	L$_s$	Local Solar Time	Date	UTC	North Latitude	East Longitude
17a, 17c	Red solid	29	163.6653	1543	26 Nov 2008	0037	−10	173
17b, 17c	Blue dashed	29	163.9391	0337	26 Nov 2008	1253	−10	173
17c, 17f	Blue solid	29	162.6877	0339	24 Nov 2008	0444	−1	−87
17d, 17f	Red dashed	29	162.9577	1541	24 Nov 2008	1652	−2	−84
17e, 17f	Blue dotted	29	163.2290	0339	25 Nov 2008	0503	−2	−82
17g, 17j	Red solid	29	165.2990	1540	29 Nov 2008	0139	7	−174
17h, 17j	Blue dashed	29	165.5703	0342	29 Nov 2008	1344	6	−170
17i, 17j	Red dotted	29	165.8448	1540	30 Nov 2008	0157	7	−169
17k, 17o	Blue dotted	29	165.7827	0338	29 Nov 2008	2311	−13	51
17l, 17o	Blue solid	29	166.0526	1545	30 Nov 2008	1112	−13	57
17m, 17o	Red dashed	29	166.3293	0338	30 Nov 2008	2330	−13	56

surface resulting in infrared cooling. (This pattern can be more complex [see *Schofield et al.*, 1997].) To a first approximation in the optically thin, plane-parallel, and nonscattering approximations, the heating rate, dT/dt, due to this effect is

$$\frac{dT}{dt} = \frac{\frac{d_*\tau}{\rho}\pi \int_0^\infty \frac{Q_{ext,\nu}}{Q_{ext,MCS}}(1-\omega_\nu)[B_\nu(T_s) - 2B_\nu(T_e)]d\nu}{c_p} \quad (23)$$

where ν denotes frequency, MCS denotes the channel in which MCS retrieves dust, ω_ν is the single scattering albedo, $B(T)$ is the Planck function, c_p is the heat capacity of the atmosphere, T_s is the temperature of the surface, and T_e is the re-emission temperature of the dust. In the daytime, T_s is ~260 K and T_e is ~200 K in the high-altitude tropical dust maximum. Assuming a high-altitude tropical maximum with a density-scaled opacity of 5×10^{-4} m^2 kg^{-1} and the parameters of the wideband model of *Hinson and Wilson* [2004], the infrared heating is 3.7 K sol^{-1}. Thus, the infrared heating is about an order of magnitude smaller than the visible heating. At night, T_s is ~200 K [*Schofield et al.*, 1997] and T_e is ~180 K, so the heating rate in the HATDM will be about −1.3 K sol^{-1}. In other words, the dust cools the atmosphere in the infrared.

[66] So within the uncertainties in the efficiency of dust absorption and the dayside profile of water ice, a zonally and diurnally averaged heating rate of 10 K sol^{-1} due to dust at 20 km above the surface is quite plausible in Mars's tropics at northern summer solstice. An average heating rate of up to 30 K sol^{-1} is possible at 30 km above the surface during early season tropical dust storm activity. Diurnal average infrared heating by water ice clouds above or roughly coincident with the HATDM may be an additional 10 K sol^{-1} or more [*Heavens et al.*, 2010]. *Medvedev and Hartogh* [2007] estimated that the zonal average tropical diabatic heating at northern summer solstice ranges from −10 to 10 K sol^{-1} in a GCM simulation without aerosol, so heating by dust and water ice may change the sign of net diabatic heating and drive a thermally direct circulation (or drive a stronger one) at higher altitudes. *Wilson et al.* [2008] have simulated such an effect by including radiatively active water ice clouds in a GCM.

5. Summary

[67] We have used MCS retrievals of temperature, dust opacity, and pressure to reconstruct the latitudinal-vertical distribution of dust during northern spring and summer and have developed a new framework for analyzing and representing the vertical distribution of dust in the atmosphere of Mars to describe its seasonal variability.

[68] We have shown the following.

[69] 1. At certain latitudes and seasons, the vertical dust distribution cannot be represented by physically plausible Conrath profiles.

[70] 2. Throughout most of northern spring and summer, the dust mass mixing ratio in the tropics tends to have a maximum at 15–25 km above the local surface: "the high-altitude tropical dust maximum." This maximum generally has a greater magnitude and altitude in the Northern Hemisphere and may have significant diurnal variability.

[71] 3. Similar maxima in mass mixing ratio sometimes occur near the north pole around the northern summer solstice.

[72] 4. There is a dust-clear zone near the pole that closely tracks the terminator and extends ~20° in latitude equatorward of it.

[73] 5. Maxima in zonal average density-scaled opacity with magnitudes 2–3 times that of the HATDM at northern summer solstice were observed at 25 to 35 km above the surface of the tropics beginning at around L_s = 145° of MY 29. These maxima were more prominent on the dayside than the nightside as northern fall equinox approached. This increase in magnitude in the HATDM coincided with "early season" tropical dust storm activity observed by THEMIS and MARCI. The HATDM appears to have been weak or absent during late northern summer of MY 28. MY 28 is thought to have been a year without early season tropical dust storm activity.

[74] 6. Diabatic atmospheric heating due to dust in the tropical atmosphere of Mars may have a maximum at greater than 15 km above the local surface. Water ice clouds above or coincident with this layer may be an additional source of infrared radiative heating.

[75] **Acknowledgments.** We thank Aymeric Spiga and an anonymous reviewer for extremely thorough and helpful reviews. The authors also would like to thank Tim McConnochie and Todd Clancy for useful discussions. This work was funded by and performed in part at the Jet Propulsion Laboratory, California Institute of Technology under contract with the National Aeronautics and Space Administration as part of the Mars Reconnaissance Orbiter project.

References

Anderson, E., and C. Leovy (1978), Mariner 9 television limb observations of dust and ice hazes on Mars, *J. Atmos. Sci.*, *35*, 723–734, doi:10.1175/1520-0469(1978)035<0723:MTLOOD>2.0.CO;2.

Barnes, J. R. (1990), Possible effects of breaking gravity waves on the circulation of the middle atmosphere of Mars, *J. Geophys. Res.*, *95*(B2), 1401–1421, doi:10.1029/JB095iB02p01401.

Benson, J. L., B. P. Bonev, P. B. James, K. J. Shan, B. A. Cantor, and M. A. Caplinger (2003), The seasonal behavior of water ice clouds in the Tharsis and Valles Marineris regions of Mars: Mars Orbiter Camera observations, *Icarus*, *165*, 34–52, doi:10.1016/S0019-1035(03)00175-1.

Cantor, B., M. Malin, and K. S. Edgett (2002), Multiyear Mars Orbiter Camera (MOC) observations of repeated Martian weather phenomena during the northern summer season, *J. Geophys. Res.*, *107*(E3), 5014, doi:10.1029/2001JE001588.

Cantor, B. A., K. M. Kanak, and K. S. Edgett (2006), Mars Orbiter Camera observations of Martian dust devils and their tracks (September 1997 to January 2006) and evaluation of theoretical vortex models, *J. Geophys. Res.*, *111*, E12002, doi:10.1029/2006JE002700.

Chassefière, E., P. Drossart, and O. Korablev (1995), Post-Phobos model for the altitude and size distribution of dust in the low Martian atmosphere, *J. Geophys. Res.*, *100*(E3), 5525–5539, doi:10.1029/94JE03363.

Clancy, R. T., B. J. Sandor, M. J. Wolff, P. R. Christensen, M. D. Smith, J. C. Pearl, B. J. Conrath, and R. J. Wilson (2000), An intercomparison of ground-based millimeter, MGS TES, and Viking atmospheric temperature measurements: Seasonal and interannual variability of temperatures and dust loading in the global Mars atmosphere, *J. Geophys. Res.*, *105*(E4), 9553–9571, doi:10.1029/1999JE001089.

Clancy, R. T., M. J. Wolff, and P. R. Christensen (2003), Mars aerosol studies with the MGS TES emission phase function observations: Optical depths, particle sizes, and ice cloud types versus latitude and solar longitude, *J. Geophys. Res.*, *108*(E9), 5098, doi:10.1029/2003JE002058.

Clancy, R. T., M. J. Wolff, B. A. Whitney, B. A. Cantor, and M. D. Smith (2007), Mars equatorial mesospheric clouds: Global occurrence and physical properties from Mars Global Surveyor Thermal Emission Spectrometer and Mars Orbiter Camera limb observations, *J. Geophys. Res.*, *112*, E04004, doi:10.1029/2006JE002805.

Clancy, R. T., M. J. Wolff, B. A. Whitney, B. A. Cantor, M. D. Smith, and T. H. McConnochie (2010), Extension of atmospheric dust loading to high altitudes during the 2001 Mars dust storm: MGS TES limb observations, *Icarus*, *207*, 98–109, doi:10.1016/j.icarus.2009.10.011.

Conrath, B. J. (1975), Thermal structure of the Martian atmosphere during the dissipation of the dust storm of 1971, *Icarus*, *24*, 36–46, doi:10.1016/0019-1035(75)90156-6.

Flasar, F. M., and R. M. Goody (1976), Diurnal behaviour of water on Mars, *Planet. Space Sci.*, *24*, 161–181, doi:10.1016/0032-0633(76)90103-3.

Forget, F., F. Hourdin, R. Fournier, C. Hourdin, O. Talagrand, M. Collins, S. R. Lewis, P. L. Read, and J.-P. Huot (1999), Improved general circulation models of the Martian atmosphere from the surface to above 80 km, *J. Geophys. Res.*, *104*, 24,155–24,175, doi:10.1029/1999JE001025.

Forget, F., Y. Wanherdrick, and S. R. Lewis (2001), Validation of the Mars General Circulation Model and Climate Database with new spacecraft observations, in *Work Package 7*, *Tech. Note 11369/95/NL/JG*, Eur. Space Agency, Paris. (Available at http://www-mars.lmd.jussieu.fr/mars/esadoc/lmd/esadoc.html.)

Gierasch, P., and R. M. Goody (1968), A study of the thermal and dynamical structure of the Martian lower atmosphere, *Planet. Space Sci.*, *16*, 615–646, doi:10.1016/0032-0633(68)90102-5.

Greeley, R., et al. (2006), Active dust devils in Gusev crater, Mars: Observations from the Mars Exploration Rover Spirit, *J. Geophys. Res.*, *111*, E12S09, doi:10.1029/2006JE002743.

Haberle, R. M., C. B. Leovy, and J. M. Pollack (1982), Some effects of global dust storms on the atmospheric circulation of Mars, *Icarus*, *50*, 322–367, doi:10.1016/0019-1035(82)90129-4.

Haberle, R. M., J. B. Pollack, J. R. Barnes, R. W. Zurek, C. B. Leovy, J. R. Murphy, J. Schaeffer, and H. Lee (1993), Mars atmospheric dynamics as simulated by the NASA/Ames general circulation model: 1. The zonal-mean circulation, *J. Geophys. Res.*, *98*, 3093–3123, doi:10.1029/92JE02946.

Hartogh, P., A. S. Medvedev, and C. Jarchow (2007), Middle atmosphere polar warmings on Mars: Simulations and study on the validation with sub-millimeter observations, *Planet. Space Sci.*, *55*(9), 1103–1112, doi:10.1016/j.pss.2006.11.018.

Hayne, P. O. (2010), Snow clouds on Mars and ice on the Moon: Infrared observations and models, Ph.D. Thesis, Univ. of Calif., Los Angeles.

Heavens, N. G., J. L. Benson, D. M. Kass, A. Kleinböhl, W. A. Abdou, D. J. McCleese, M. I. Richardson, J. T. Schofield, J. H. Shirley, and P. M. Wolkenberg (2010), Water ice clouds over the Martian tropics during northern summer, *Geophys. Res. Lett.*, *37*, L18202, doi:10.1029/2010GL044610.

Heavens, N. G., M. I. Richardson, A. Kleinböhl, D. M. Kass, D. J. McCleese, W. Abdou, J. L. Benson, J. T. Schofield, J. H. Shirley, and P. M. Wolkenberg (2011), Vertical distribution of dust in the Martian atmosphere during northern spring and summer: High-altitude tropical dust maximum at northern summer solstice, *J. Geophys. Res.*, *116*, E01007, doi:10.1029/2010JE003692.

Hinson, D. P., and R. J. Wilson (2004), Temperature inversions, thermal tides, and water ice clouds in the Martian tropics, *J. Geophys. Res.*, *109*, E01002, doi:10.1029/2003JE002129.

Jaquin, F., P. Gierasch, and R. Kahn (1986), The vertical structure of limb hazes in the Martian atmosphere, *Icarus*, *72*, 528–534.

Kahre, M. A., J. R. Murphy, and R. M. Haberle (2006), Modeling the Martian dust cycle and surface dust reservoirs with the NASA Ames general circulation model, *J. Geophys. Res.*, *111*, E06008, doi:10.1029/2005JE002588.

Kahre, M. A., J. L. Hollingsworth, R. M. Haberle, and J. R. Murphy (2008), Investigations of dust particle sizes in the Martian atmosphere using the NASA Ames General Circulation Model, *Icarus*, *195*, 576–597, doi:10.1016/j.icarus.2008.01.023.

Kleinböhl, A., et al. (2009a), Mars Climate Sounder limb profile retrieval of atmospheric temperature, pressure, dust, and water ice opacity, *J. Geophys. Res.*, *114*, E10006, doi:10.1029/2009JE003358.

Kleinböhl, A., W. A. Abdou, J. T. Schofield, D. M. Kass, and D. J. McCleese (2009b), Mars Climate Sounder limb retrievals of dust and water ice using scattering radiative transfer: Implications for particle size, paper presented at Mars Dust Cycle Workshop, NASA Ames Res. Cent., Mountain View, Calif., 15–17 Sept.

Lee, S. W., P. C. Thomas, and J. Veverka (1982), Wind streaks in Tharsis and Elysium—Implications for sediment transport by slope winds, *J. Geophys. Res.*, *87*, 10,025–10,041, doi:10.1029/JB087iB12p10025.

Lemmon, M. T., et al. (2004), Atmospheric imaging results from the Mars exploration rovers: Spirit and Opportunity, *Science*, *306*, 1753–1756, doi:10.1126/science.1104474.

Leovy, C. (1982), Martian meteorological variability, *Adv. Space Res.*, *2*, 19–44, doi:10.1016/0273-1177(82)90103-X.

Malin, M. C., B. A. Cantor, T.N. Harrison, D.E. Shean and M. R. Kennedy (2008), MRO MARCI Weather Report for the week of 10 November 2008–16 November 2008, Malin Space Science Systems Captioned Image Release, MSSS-59, http://www.msss.com/msss_images/2008/11/19/.

Malin, M. C., B. A. Cantor, T.N. Harrison, D.E. Shean and M. R. Kennedy (2009), MRO MARCI Weather Report for the week of 13 July 2009–19 July 2009, Malin Space Science Systems Captioned Image Release, MSSS-92, http://www.msss.com/msss_images/2009/07/22/.

Martin, L. J., and R. W. Zurek (1993), An analysis of the history of dust activity on Mars, *J. Geophys. Res.*, *98*, 3221–3246, doi:10.1029/92JE02937.

McCleese, D. J., J. T. Schofield, F. W. Taylor, S. B. Calcutt, M. C. Foote, D. M. Kass, C. B. Leovy, D. A. Paige, P. L. Read, and R. W. Zurek (2007), Mars Climate Sounder: An investigation of thermal and water vapor structure, dust and condensate distributions in the atmosphere, and energy balance of the polar regions, *J. Geophys. Res.*, *112*, E05S06, doi:10.1029/2006JE002790.

McCleese, D. J., et al. (2008), Intense polar temperature inversion in the middle atmosphere on Mars, *Nat. Geosci.*, *1*, 745–749, doi:10.1038/ngeo332.

McCleese, D. J., et al. (2010), Structure and dynamics of the Martian lower and middle atmosphere as observed by the Mars Climate Sounder: Seasonal variations in zonal mean temperature, dust, and water ice aerosols, *J. Geophys. Res.*, *115*, E12016, doi:10.1029/2010JE003677.

McConnochie, T. H., J. F. Bell III, D. Savransky, M. J. Wolff, A. D. Toigo, H. Wang, M. I. Richardson, and P. R. Christensen (2010), THEMIS-VIS observations of clouds in the Martian mesosphere: Altitudes, wind speeds, and decameter-scale morphology, *Icarus*, *210*, 545–565, doi:10.1016/j.icarus.2010.07.021.

Medvedev, A. S., and P. Hartogh (2007), Winter polar warmings and the meridional transport on Mars simulated with a general circulation model, *Icarus*, *186*(1), 97–110, doi:10.1016/j.icarus.2006.08.020.

Möhlmann, D. T. F., M. Niemand, V. Formisano, H. Savijärvi, and P. Wolkenberg (2009), Fog phenomena on Mars, *Planet. Space Sci.*, *57*(14–15), 1987–1992, doi:10.1016/j.pss.2009.08.003.

Montmessin, F., F. Forget, P. Rannou, M. Cabane, and R. M. Haberle (2004), Origin and role of water ice clouds in the Martian water cycle as inferred from a general circulation model, *J. Geophys. Res.*, *109*, E10004, doi:10.1029/2004JE002284.

Montmessin, F., E. Quemerais, J. L. Bertaux, O. Korablev, P. Rannou, and S. Lebonnois (2006), Stellar occultations at UV wavelengths by the SPICAM instrument: Retrieval and analysis of Martian haze profiles, *J. Geophys. Res.*, *111*, E09S09, doi:10.1029/2005JE002662.

Montmessin, F., B. Gondet, J.-P. Bibring, Y. Langevin, P. Drossart, F. Forget, and T. Fouchet (2007), Hyperspectral imaging of convective CO_2 ice clouds in the equatorial mesosphere of Mars, *J. Geophys. Res.*, *112*, E11S90, doi:10.1029/2007JE002944.

Murphy, J. R., O. B. Toon, R. M. Haberle, and J. B. Pollack (1990), Numerical simulations of the decay of Martian global dust storms, *J. Geophys. Res.*, *95*(B9), 14,629–14,648, doi:10.1029/JB095iB09p14629.

Nelli, S. M., and J. R. Murphy (2002), Interrelationship between the dust and water cycles in the Martian atmosphere: Numerical modeling studies, paper presented at the 200th Meeting of the American Astronomical Society, Albuquerque, N. M., June.

Rafkin, S. C. R., M. R. V. Sta. Maria, and T. I. Michaels (2002), Simulation of the atmospheric thermal circulation of a Martian volcano using a mesoscale numerical model, *Nature*, *419*, 697–699, doi:10.1038/nature01114.

Rannou, P., S. Perrier, J.-L. Bertaux, F. Montmessin, O. Korablev, and A. Rébérac (2006), Dust and cloud detection at the Mars limb with UV scattered sunlight with SPICAM, *J. Geophys. Res.*, *111*, E09S10, doi:10.1029/2006JE002693.

Richardson, M. I. (1998), Comparison of microwave and infrared measurements of Martian atmospheric temperatures: Implications for short-term climate variability, *J. Geophys. Res.*, *103*(E3), 5911–5918, doi:10.1029/97JE03372.

Rind, D., and W. B. Rossow (1984), The effects of physical processes on the Hadley circulation, *J. Atmos. Sci.*, *41*(4), 479–507, doi:10.1175/1520-0469(1984)041<0479:TEOPPO>2.0.CO;2.

Schneider, E. K. (1983), Martian great dust storms: Interpretive axially symmetric models, *Icarus*, *55*, 302–331, doi:10.1016/0019-1035(83)90084-2.

Schofield, J. T., J. R. Barnes, D. Crisp, R. M. Haberle, S. Larsen, J. A. Magalhaes, J. R. Murphy, A. Seiff, and G. Wilson (1997), The Mars Pathfinder Atmospheric Structure Investigation/Meteorology (ASI/MET) experiment, *Science*, *278*(5344), 1752–1758, doi:10.1126/science.278.5344.1752.

Smith, M. D. (2004), Interannual variability in TES atmospheric observations of Mars during 1999–2003, *Icarus*, *167*(1), 148–165, doi:10.1016/j.icarus.2003.09.010.

Smith, M. D. (2009), THEMIS observations of Mars aerosol optical depth from 2002–2008, *Icarus*, *202*(2), 444–452, doi:10.1016/j.icarus.2009.03.027.

Smith, M. D., J. C. Pearl, B. J. Conrath, and P. R. Christensen (2001), Thermal Emission Spectrometer results: Mars atmospheric thermal structure and aerosol distribution, *J. Geophys. Res.*, *106*, 23,929–23,945, doi:10.1029/2000JE001321.

Tamppari, L. K., R. W. Zurek, and D. A. Paige (2003), Viking-era diurnal water-ice clouds, *J. Geophys. Res.*, *108*(E7), 5073, doi:10.1029/2002JE001911.

Tao, W.-K., S. Lang, W. S. Olson, R. Meneghini, S. Yang, J. Simpson, C. Kummerow, E. Smith, and J. Halverson (2001), Retrieved vertical profiles of latent heat release using TRMM rainfall products for February 1998, *J. Appl. Meteorol.*, *40*, 957–982, doi:10.1175/1520-0450(2001)040<0957:RVPOLH>2.0.CO;2.

Taylor, P. A., P.-Y. Li, D. V. Michelangeli, J. Pathak, and W. Weng (2007), Modelling dust distributions in the atmospheric boundary layer on Mars, *Boundary Layer Meteorol.*, *125*(2), 305–328, doi:10.1007/s10546-007-9158-9.

Wang, H., and A. P. Ingersoll (2002), Martian clouds observed by Mars Global Surveyor Mars Orbiter Camera, *J. Geophys. Res.*, *107*(E10), 5078, doi:10.1029/2001JE001815.

Wang, J., and W. B. Rossow (1998), Effects of cloud vertical structure on atmospheric circulation in the GISS GCM, *J. Clim.*, *11*, 3010–3029, doi:10.1175/1520-0442(1998)011<3010:EOCVSO>2.0.CO;2.

Wilson, R. J., and K. Hamilton (1996), Comprehensive model simulation of thermal tides in the Martian atmosphere, *J. Atmos. Sci.*, *53*, 1290–1326, doi:10.1175/1520-0469(1996)053<1290:CMSOTT>2.0.CO;2.

Wilson, R. J., and M. I. Richardson (2000), The Martian atmosphere during the Viking mission, part I, Infrared measurements of atmospheric temperatures revisited, *Icarus*, *145*, 555–579, doi:10.1006/icar.2000.6378.

Wilson, R. J., S. R. Lewis, L. Montabone, and M. D. Smith (2008), Influence of water ice clouds on Martian tropical atmospheric temperatures, *Geophys. Res. Lett.*, *35*, L07202, doi:10.1029/2007GL032405.

Wolff, M. J., and R. T. Clancy (2003), Constraints on the size of Martian aerosols from Thermal Emission Spectrometer observations, *J. Geophys. Res.*, *108*(E9), 5097, doi:10.1029/2003JE002057.

Zurek, R. W., J. R. Barnes, R. M. Haberle, J. B. Pollack, J. E. Tillman, and C. B. Leovy (1992), Dynamics of the atmosphere of Mars, in *Mars*, edited by H. H. Kieffer et al., pp. 835–933, Univ. of Ariz. Press, Tucson.

W. Abdou, J. L. Benson, D. M. Kass, A. Kleinböhl, D. J. McCleese, J. T. Schofield, J. H. Shirley, and P. M. Wolkenberg, Jet Propulsion Laboratory, California Institute of Technology, 4800 Oak Grove Dr., Pasadena, CA 91109, USA.

N. G. Heavens, Department of Earth and Atmospheric Sciences, Cornell University, 1118 Bradfield Hall, Ithaca, NY 14853, USA. (heavens@cornell.edu)

M. I. Richardson, Ashima Research, 600 S. Lake Ave., Suite 303, Pasadena, CA 91106, USA.